Optical components based on high index materials

Andersen, Karin Nordström

Publication date:
2005

Document Version
Publisher's PDF, also known as Version of record

Optical components based on high index materials

Karin Nordström Andersen

March 31st, 2005

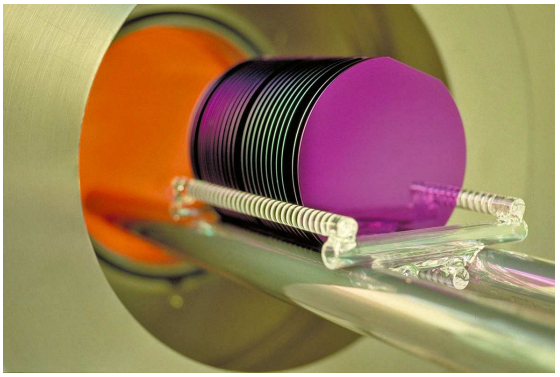

Research Center COM
Technical University of Denmark
Building 345V
2800 Kgs. Lyngby
DENMARK

Contents

Preface

The work presented in this thesis is submitted in order to obtain the Ph.D. degree at the Technical University of Denmark (DTU).

The work was initiated in October 2002 and completed in March 2005 at the Research Center for Communication, Optics, and Materials (COM). Originally, Winnie Svendsen served my as main supervisor and Karsten Rottwitt as co-supervisor; when in September 2003 Winnie Svendsen left to pursue opportunities elsewhere, Karsten Rotwitt took over the role as main supervisor, with Mogens Rysholt Poulsen as co-supervisor.

As part of my Ph.D. program I have spent six months at Institut für Physik at Universität der Bundeswehr München in Germany under the supervision of Hermann Baumgärtner. Three weeks was spent at RISØ National Laboratory in Denmark and at HASYLAB in Germany collaborating with Martin Meedom Nielsen. I also had the pleasure of spending two weeks at the University of Twente in the Netherlands working with the Integrated Optical Micro Systems Group.

Abstract

This thesis is part of a Ph.D. project: "Optical components based on high index materials", carried out at COM at the Technical University of Denmark. The project has focused on the material and optical characterization of silicon rich nitride (SRN) thin films and waveguides, with the goal of developing efficient and reliable fabrication methods for submicron optical components for use in high-speed optical telecommunications. Some of the results are described in more detail in previously published papers.

The work has been divided into three parts: thin film characterization, cleanroom fabrication, and analysis waveguide components. The thin film characteristics and the cleanroom fabrication strongly influence the performance of optical waveguide components. Hence, the thin film properties and waveguide fabrication have been developed and reoptimized for the best optical performance.

The first part of the work is material and optical characterization of the thin films. It consists of determination of stoichiometry, chemical composition, and optical loss of SRN film films. Most of this part of the work was performed at the Universität der Bundeswehr München, Germany, and the University of Twente, the Netherlands.

The second part is fabrication of optical submicron structures in SRN films. The cleanroom fabrication was optimized in such a way as to minimize the optical losses in the waveguide structures and maximize the overall production efficiency. A process has been developed for processing submicron structures with UV-photolithography and reactive ion etching. The components have vertical sidewalls with a roughness small enough not to induce scattering losses. The processing steps are optimized so as to produce a reliable processing sequence for making low loss single mode waveguide components.

The third part is an analysis of SRN waveguides and components. The main focus has been on minimizing the optical losses resulting from the production of waveguide structures in the SRN thin films. New and yet unpublished results show that a process optimization and a reduction of the number of particles has reduced the propagation loss to a degree where no extra loss is induced, compared to the losses in the thin film itself. In addition, the performance of a ring resonator has been investigated. It was possible to achieve a free spectral range that is larger than the channel spacing in wavelength division multiplexing (WDM) systems. This allows for the selection of a single wavelength band within the complete telecommunication C-band (1530 - 1570 nm).

Dansk resumé

Denne afhandling beskriver et Ph.d.-projekt med titlen: "Optiske komponenter baseret på høj indeks materialer", udført på COM ved Danmarks Tekniske Universitet. Arbejdet er hovedsageligt koncentreret om karakterisering af silicium-nitrid tyndfilm og bølgeledere og fremstilling af submikrometer optiske komponenter. Det langsigtede mål er at fremstille integrerede komponenter til optisk signalprocessering i forbindelse med optisk telekommunikation. Delresultater fra projektet er nærmere beskrevet i separate publikationer i tidsskrifter og konferencerapporter.

Projektet er opdelt i tre hovedpunkter: renrumsprocessering, materialeanalyse og optiske egenskaber. Disse tre punkter, som er uddybet nedenstående, er alle tæt knyttet, idet renrumsprocesseringen og materialeegenskaberne har stor indflydelse på de optiske egenskaber. Når man ved præcist, hvordan de enkelte parametre ændrer de optiske egenskaber, er det muligt at forbedre både proceseringen og materialerne og derved fremme bestemte optiske egenskaber.

Det første punkt omhandler optimering af renrumsprocesserne, hovedsagelig fotolithografi og reaktiv ion ætsning, herunder undersøgelse af blandt andet liniebreddereduktion og ruhed af bølgelederne. Renrumsprocesseringen omfatter også selve deponeringen af kernelaget. Deponeringsbetingelser, defekter, ruhed af bølgeledere, annealing osv. har alle indflydelse på de optiske tab i bølgelederkomponenterne, så det er vigtigt at forstå tabsmekanismernes afhængighed af processeringen for at forbedre komponenternes egenskaber. Liniebreddereduktion og ruhed bestemmes ved hjælp af skanning elektron mikroskopi.

Materialeanalysen udgør en anden og meget vigtig del. Det har vist sig, at der i materialet kan optræde N-H bindinger med absorption i bølgelængdeområdet for optisk kommunikation. For at bryde disse bind-

inger skal filmen udglødes ('anneales', dvs. opvarmes til meget høj temperatur), men dette har vist sig at føre til dannelsen af klynger (krystalinske faser), som medfører øget spredning af lyset. Målet med materialeanalysen er at finde en passende balance mellem fjernelse af N-H bindinger og samtidig minimering af klyngedannelsen.

For at analysere stoichiometrien, de kemiske bindinger, urenheder og krystallinske faser i det ellers amorfe materiale har jeg brugt røntgen fotoelektron spectroskopi (XPS) og røntgendiffraktion. De indledende forsøg blev lavet i samarbejde med Forskningscenter Risø. Den mere specifikke karakterisering har jeg lavet under mine udlandsophold på Institut für Physik ved Universität der Bundeswehr München og Twente Universitet. Her lavede jeg Rutherford tilbagesprednings spektroskopi for at bestemme den kvalitative stoichiometri af prøver proccesseret under forskellige deponerings - og annealingsbetingelser. Jeg udførte også XPS for at undersøge, hvilke kemiske forbindelser der var i mine tyndfilm. Endelig har jeg også undersøgt de fremstillede komponenter med transmissions elektronmikroskopi.

Det sidste punkt er selve de optiske egenskaber af bølglederkomponenterne. Jeg undersøgte, hvordan disse egenskaber afhænger af renrumsprocesseringen (bølgelederruhed, deponeringsparametre, annealingsparametre osv.) og af materialeegenskaberne (dvs. stoichiometri, kemiske bindinger, krystallinske faser o. l.). Derudover blev der lavet forsøg med en ring-resonator, hvor koblingen mellem to bølgeledere blev undersøgt. Der blev observeret en spektral afstand på over 30 nm, hvilket er større end afstanden mellem to kanaler i bølgelængde divisions multipleks systemer. Det vil sige, at det er muligt at udvælge enkelte bølgelængdebånd inden for hele telekommunikations C-båndet (1530 - 1570 nm). Brydningsindekset for traditionelle kernelag, så som silica eller silicium oxinitrid, er for lavt til at de spektrale afstande kan blive store nok til at skelne mellem to kanaler. En af de helt store fordele ved at bruge silicium rig nitrid som kernelag er netop, at den spektrale afstand mellem kanalerne kan gøres så stor, at næsten arbitrære filter funktioner kan designes ud fra nogle få simple byggeblokke.

Acknowledgements

I owe a great many thanks to a lot of people in Denmark, Germany, and the Netherlands.

First of all I would like to thank Winnie Svendsen for giving a wonderful start on my Ph.D. project, for always being there through good and bad times, and for continuing the collaboration after changing research field.

A special thanks to my supervisors Karsten Rottwitt and Mogens Rysholt Poulsen for support and inspiring discussions.

I would like to thank Jörg Hübner for introducing me to the world of integrated optics, Peter Carøe Nielsen for collaboration on the initial cleanroom processing, Hugh Philipp for component design, Haiyan Ou for feedback on cleanroom fabrication, Hans Mertens for dual prism coupling and FTIR measurements, Martin Meedom Nielsen for synchrotron radiation measurements, Jacques Chevallier for TEM sample preparation and analysis, Peixiong Shi for SIMS measurements, the DANCHIP staff for providing an excellent work environment, and Christian Mikkelsen, Rasmus Kousholt Sandberg, and Dan Zauner for their support and weird discussions during lunch.

A special thanks to director Anders Bjarklev, the former ILC group, the nanophotonics group, and the rest of COM for providing a good frame for my work.

Thanks to Institut für Physik, Universität der Bundeswehr München for providing the material analysis equipment and for giving me free German lessons during lunch and seminars. Thanks to Hermann Baumgärtner, Ignaz Eisele, and Jörg Schultz for giving me a warm welcome and an enjoyable stay. Thanks to Tanja Stimpel-Lindner and Vanessa Capodieci for valuable discussions on XPS, to Torsten Sulima for showing me the

fun world of RBS, and to Markus Schindler for helping out with spectral ellipsometry.

The Integrated Optical Micro Systems Group at University of Twente is acknowledged for making my stay an interesting and inspiring one.

I greatly appreciate the suggestions and corrections to this manuscript from Winnie Svendsen, Karsten Rottwitt, Mogens Rysholt Poulsen, Rune Shim Jacobsen, Dan Zauner, and Johannes Andersen.

Last but not least, I would like to thank my parents, my sister, my brother, Helle Knudsen, Mette Bie Andersen, Lars Lindberg Christensen, Eyvind Joensen, and the rest of my friends for their full support during my Ph.D. studies.

Ph.D. Publications

The following publications have resulted from this Ph.D. project.

[A] K. N. Andersen, W. E. Svendsen, T. Stimpel-Lindner, T. Sulima, and H. Baumgärtner. "Annealing and deposition effects of the chemical composition of silicon-rich nitride", *Applied Surface Science*, vol. 243, no. 1-4, pp. 403–410, 2005

[B] H. T. Philipp, H. J. Deyerl, K. N. Andersen, K. Færch, H. Ou, J. Hübner, and W. Svendsen. "UV-written gratings for high-index contrast amorphous silicon nitride waveguides", *submitted to Photonics Technology Letters*, 2004

[C] K. N. Andersen, W. E. Svendsen, T. Stimpel-Lindner, T. Sulima, H. Baumgärtner, and H. Philipp. "Annealing and deposition effects on the chemical composition of silicon rich nitride", in *DFS annual meeting,* p. FF22P, 2004

[D] K. N. Andersen, W. E. Svendsen, T. Stimpel-Lindner, T. Sulima, H. Baumgärtner, and H. Philipp. "Annealing and deposition effects on the chemical composition of silicon rich nitride", in *KIF annual meeting,* p. KF04P, 2004

[E] H. T. Philipp, K. N. Andersen, W. Svendsen, and H. Ou. "Low-loss silicon rich nitride waveguides for high density integrated optics", in *Integrated Photonic Research/Optical Society of America,* p. JWB28, 2004

[F] H. Philipp, K. Andersen, W. Svendsen, and H. Ou. "Amorphous silicon rich silicon nitride optical waveguides for high density integrated optics", *Electronics Letters*, vol. 40, no. 7, pp. 419–420, 2004

[G] H. T. Philipp, K. N. Andersen, W. E. Svendsen, and M. Svalgaard. "High-density high-index contrast integrated optics developments and applications at COM", *DOPS-NYT*, vol. 19, no. 1, pp. 10–14, 2004

[H] H. T. Philipp, W. Svendsen, K. N. Andersen, J. Hübner, and J. Hedegaard Povlsen. "Measurement of optical nonlinearity in silicon rich nitride waveguide ring resonators", *Electronics Letters*, vol. 39, no. 16, pp. 1184–1185, 2003

[I] K. N. Andersen, W. E. Svendsen, R. K. Sandberg, H. T. Philipp, and J. Hübner. "Silicon rich nitride micro-resonators", *11th European Conference on Integrated Optics*, vol. 1, pp. 43–6, 2003

[J] K. Rottwitt, M. Dyndgaard, K. Andersen, and T. Hansen. "Submicrometer waveguide for nano-optics", in *Lasers and Electro-Optics Europe, CLEO/Europe,* p. 696, 2003

[K] K. N. Andersen, W. Svendsen, and H. Philipp. "Silicon rich nitride micro-resonators for optical filters", in *DFS annual meeting,* p. FF25P, 2003

[L] K. N. Andersen, P. C. Nielsen, and W. Svendsen. "Silicon rich nitride thin films and waveguides", in *Integrated Photonic Research/Optical Society of America,* IThA4, pp. 1–3, 2002

[M] H. Mertens, K. N. Andersen, and W. Svendsen. "Optical loss analysis of silicon rich nitride waveguides", in *ECOC'02,* Copenhagen, Denmark, Paper P1.38, 2002

[N] W. Svendsen, H. T. Philipp, H. Svalgaard, M. Mertens, and K. N. Andersen. "High index ring resonator coupled to uv-written wave-

guide", in *ECOC'02,* Copenhagen, Denmark, Paper 4.2.4, 2002

[O] K. N. Andersen. "Integrated optical components and materials", in *KIF annual meeting,* p. KF02, 2002

[P] H. Mertens, W. Svendsen, K. N. Andersen, and H. Philipp. "Optical loss analysis of silicon rich nitride waveguides and their applications", in *DFS annual meeting,* p. FF70P, 2002

[Q] K. N. Andersen, P. C. Nielsen, H. Philipp, and H. Mertens. "Silicon rich nitride and components", in *DOPS annual meeting,* 2001

List of Figures

Chapter 1

Introduction

Signal transmission via optical fibres is the technology of choice in high-speed telecommunications. The current bottleneck is the signal processing at the transmitting and receiving ends, which involves converting slow electrons to fast photons or vice versa. Substantial speed gains are possible if the entire signal processing can be done directly with photons, avoiding the slow conversion to electrons, especially if this can be done in small, integrated optical components, analogous to present-day integrated electronic components, but much faster. This thesis project represents a step towards this goal.

Currently, the dominant fabrication method for integrated optical waveguides relies upon silica-on-silicon technology. However, devices using this technology are large - particularly when compared to integrated electronic devices. The reason for this is that the refractive index profile has been optimized for coupling to standard optical fibers. Choosing such an index profile means a minimum allowable radius of curvature on the order of centimeters, in order to ensure low power loss. This makes complex optical circuits very large, impossible to implement as monolithic devices.

There is a concentrated effort in the industry to reduce the size of integrated optical devices. One way to do this is to increase the refractive index step (the difference in refractive index between the core and cladding) in optical waveguides. A higher refractive index step allows waveguides to make sharper bends while retaining good optical transmission. Sharper bends, in turn, make more compact and complex devices

possible.

In this thesis the refractive index is referred to as index; similarly, a refractive index step will be referred to as an index step. A high index of a material is understood as referred to silica, and an index step is referred to as the difference in index between the core material and the silica cladding.

All of the thicknesses and indexes in this thesis are measured by ellipsometry and/or prism coupling. With the ellipsometer it is possible to measure the index with light of a wavelength from 300 to 700 nm, and with the prism coupler the wavelengths are 633 nm and 1550 nm. The advantage of using the ellipsometer is that it is possible to program the measurement such that the index and thickness is measured automatically several places on the same wafer. The advantage of the prism coupler is the much better accuracy, and the index is measured at the wavelength of telecommunication.

Digital optical filters are a major field of interest, because of the fact that nearly arbitrary filter functions can be built out of a few rather simple building blocks using digital signal processing technology [1]. One of the main disadvantages in realizing these filters has been the limitation in bending radius, leading to large and expensive components with a limited free spectral range (FSR) of the filter. Using a material with a high refractive index as waveguide material, ring resonators can be realized with bend radii smaller by a factor of a hundred than those normally used in silica based components. This means that the required area for one resonator loop is nearly four orders of magnitude smaller, allowing a much higher integration density of the optical components. Another advantage is that the high index allows for a larger FSR than channel spacing in wavelength division multiplexing (WDM) systems. This allows for the selection of a single wavelength band within the complete telecommunication C-band (1530 - 1570 nm).

Low stress silicon rich nitride (SRN) is a very well suited material for integrated optics, due to the excellent uniformity of thickness and refractive index, reproducibility and tenability. The index of SRN is much higher than silica, allowing smaller bending radii and larger FSR when making optical components. The typical bending radius for silica waveguides is of the order of centimeters, which results in a FSR of around 0.01 nm [2] and [3]. This value is much too small to be of use in WDM

systems. SiON can have a refractive index varying from that of silica to that of Si_3N_4. In principle, the FSR obtained with the highest index of this material could be close to that of SRN, but for practical reasons most researchers choose a refractive index that is much lower than that and therefore the FSR achieved is of around 2 nm [4], [5]. Going to the other extreme, increasing the refractive index to that of for example silicon gives experimentally observed FSR values of around 20 nm [6], [7]. This is close to that achievable with SRN, but the processing tolerances are much tighter.

Traditionally, silicon nitride has been used for etch masks, passivation layers, and diffusion barriers (see for example [8] and [9]) due to the high density, thermal stability, resistance to moisture penetration, and chemical inertness of the material. The material characteristics of SRN strongly influence the optical properties, and it is therefore very important to know the exact characteristics in order to fine-tune the material for optimum performance.

The main purpose of this Ph. D. work was to characterize the material and optical properties of SRN thin films and fabricate and analyze SRN waveguides and components. The main focus was on the reduction of the propagation loss in thin films and optical waveguides. The influence of the thin film characteristics and the cleanroom fabrication on the optical performance has been developed and optimized.

1.1 Outline of the thesis

This thesis is divided into seven chapters (including this introduction):

Chapter 2 is dedicated to a description of the fabrication of optical submicron structures in SRN films. The cleanroom processing was optimized in such a way as to minimize the optical losses in single mode waveguide structures. The cleanroom referred to in this thesis is the DANCHIP micro- and nanotechnology processing facility at the Technical University of Denmark (DTU).

In chapter 3 the material characterization of SRN thin films is addressed. It describes the determination of stoichiometry and chemical composition of SRN thin films when different deposition and annealing conditions are applied.

Chapter 4 deals with optical characterization of SRN thin films with

the main emphasis on reducing the optical losses in the wavelength region of telecommunication.

The analysis of SRN waveguides is described in chapter 5. With the knowledge from the previous three chapters the optical losses due to thin film and fabrication effects are compared. Also the influence of annealing temperature on the losses is investigated.

An example of a component with an SRN core layer is investigated in chapter 6. The coupling between waveguides and the properties of ring resonator configurations are described.

The main results achieved during the project are summarized in chapter 7.

Chapter 1 references

[1] C. K. Madsen and J. H. Zhao. *Optical Filter Design and Analysis: A Signal Processing Approach*. Microwave and Optical Engineering. John Wiley & Sons, Inc., July 1999. ISBN 0-471-18373-3.

[2] C. Laurent-Lund. *Multilevel integration of Optical Waveguides*. Ph.d. thesis, MIC, DTU, Denmark, august 1997. ISBN 87-89935-10-1.

[3] S. Suzuki, K. Shuto, and Y. Hibino. "Integrated-optic ring resonators with two stacked layers of silica waveguide on Si", *IEEE Photonics Technology Letters*, vol. 4, no. 11, pp. 1256–1258, 1992.

[4] R. M. deRidder, K. Warhoff, A. Driessen, P. V. Lambeck, and H. Albers. "Silicon oxynitride planar waveguiding structures for application in optical communication", *IEEE Journal on Selected Topics in Quantum Electronics*, vol. 4, no. 6, pp. 930–937, 1998.

[5] F. Horst, R. Beyeler, G. L. Bona, R. Germann, B. Offrein, C. G. H. Roeloffzen, H. W. M. Salemink, and D. Wiesmann. "SiON-based integrated optics devices for WDM networks", *Lasers and Electro-Optics Society 2000 Annual Meeting. LEOS 2000. 13th Annual Meeting. IEEE*, vol. 2, pp. 756–757, 2000.

[6] W. R. Headley, G. T. Reed, A. Liu, M. Paniccia, and S. Howe. "Polarisation independent optical ring resonators on silicon on insulator", *Integrated Optics and Photonic Integrated Circuits and Proceedings of SPIE - The International Society for Optical Engineering*, vol. 5451, pp. 276–283, 2004.

[7] P. Dumon, W. Bogaerts, V. Wiaux, J. Wouters, S. Beckx, J. Van Campenhout, D. Taillaert, B. Luyssaert, P. Bienstman, D. Van Thourhout, and R. Baets. "Low-loss soi photonic wires and ring resonators fabricated with deep uv lithography", *Photonics Technology Letters, IEEE*, vol. 16, no. 5, pp. 1328–1330, 2004.

[8] E. A. Joseph, B. Zhou, S. P. Sant, L. J. Overzet, and M. J. Goeckner. "Investigation and modeling of plasma-wall interactions in inductively coupled fluorocarbon plasmas", *Journal of Vacuum Science and Technology A: Vacuum, Surfaces and Films*, vol. 22, no. 3, pp. 689–697, 2004.

[9] B. Rousset, L. Furgal, P. Fadel, A. Fulop, D. Pujos, and P. Temple-Boyer. "Development of SiN_x LPCVD processes for microtechnological applications", *Journal De Physique. IV : JP*, vol. 11, no. 3, pp. Pr3937–Pr3944, 2001.

Chapter 2

Fabrication of High Index Optical Components

The goal of this project regarding the fabrication of high refractive index compact optical components is to develop a stable and relatively cost efficient process for producing low loss submicron waveguides, using the equipment available in the cleanroom.

The processing sequence for silicon rich nitride (SRN) waveguide structures is described in detail in this chapter. The most critical step is making submicron structures using UV-photolithography, because the feature dimensions are just at the limit of what is possible within the limitations of the aligner wavelength. Each step has been carefully optimized to give the best result at the final stage of the processing sequence. In short, the steps are as follows (see figure 2.1):

First, clean silicon wafers are thermally oxidized. The oxide layer should have a thickness of a minimum of 6 μm. This thickness was chosen such that the oxide layer could be used as a buffer layer for SRN waveguides with a good confinement and negligible leakage of light into the substrate. The quality of this oxide layer is checked for refractive index, thickness uniformity, and contaminating (number of particles). If all the parameters are satisfactory one can proceed to the next step, which is the deposition of the core layer.

The core layer, which is SRN, is deposited in a low-pressure chemical vapor deposition (LPCVD) nitride oven. The recipe is a silicon rich deposition run with a gas flow ratio of 3 between dichlorosilane (DCS),

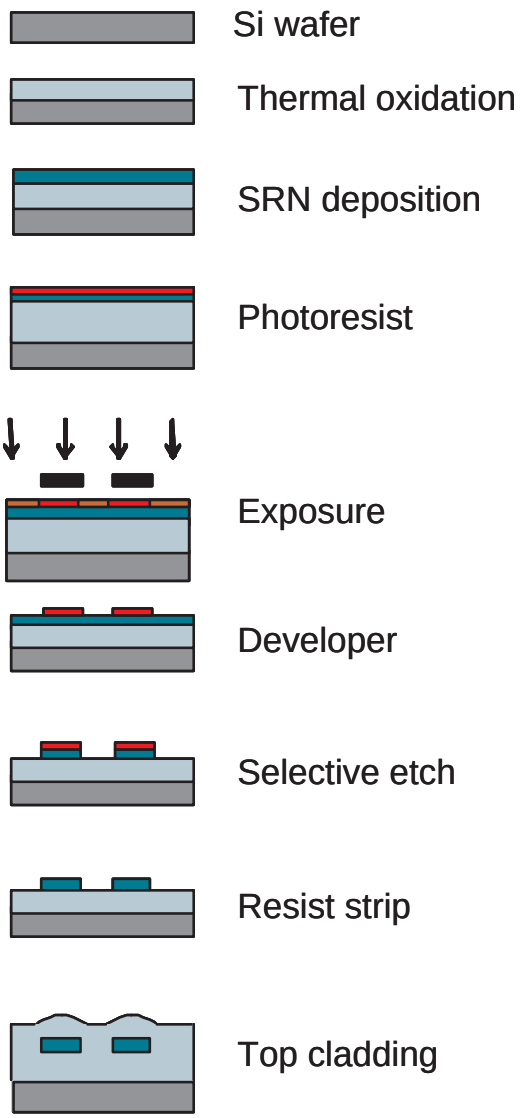

Figure 2.1: The processing sequence for SRN waveguide structures. From the top to bottom, first clean silicon wafers are thermally oxidized, SRN is deposited on top, and then photolithography is performed. By selective etching the SRN structures are transferred from the masking material onto SRN. Finally the waveguides are covered by top cladding.

Cl_2SiH_4, and ammonia, NH_3, a low pressure of ($<$ 200 mTorr), a high temperature ($>$700 °C), and a deposition time of two hours (excluding the time to ramp the temperature and gas flows up and down). This gives an SRN thin film with a thickness of 0.6 μm and a measured refractive index of 2.09 at 633 nm and 2.06 at 1550 nm using the prism coupling technique. If the uniformity of the thickness and index and the number of particles are acceptable, the core layer is ready to be annealed. This step is included in order to break any N-H bonds, which have an absorption overtone frequency of 1524 nm, thereby reducing the propagation losses in the C-band for optical telecommunication. The wafers are annealed at 1100 °C in N_2 for 4 hours. Once again the uniformity of the thickness and index and the number of particles is monitored.

The next step is to pattern the core layer to make optical components. This is done by UV-photolithography, followed by post baking of the resist for one hour. This is the most critical step in the processing of waveguides since it defines the waveguide widths, bends, holes, and other features. On each chip on the masks there is a set of test patterns, which can be used to monitor the quality of these features (an example is shown in figure 2.2). The test patterns are inspected by optical microscopy and scanning electron microscopy (SEM).

Once the component structures are well defined by the photoresist, they are ready to be transferred onto the SRN by reactive ion etching (RIE). When the structures are successfully transferred from the photoresist onto the SRN, the components are covered by a top cladding consisting of boron and phosphorous doped glass, which is then annealed in order to make the glass flow and cover the structures completely.

The following sections describe each step in detail. Section 2.1 describes the thermal oxidation of silicon wafers, section 2.2 deals with deposition of SRN thin films, section 2.3 explains the photolithography steps, section 2.4 the selective etching of SRN, and the top cladding is discussed in section 2.5.

2.1 Thermal oxidation

The buffer layer used for optical components is often silicon dioxide with a refractive index of 1.458 measured by prism coupling with a light source of a wavelength of 633 nm (1.445 at a wavelength of 1550 nm). This

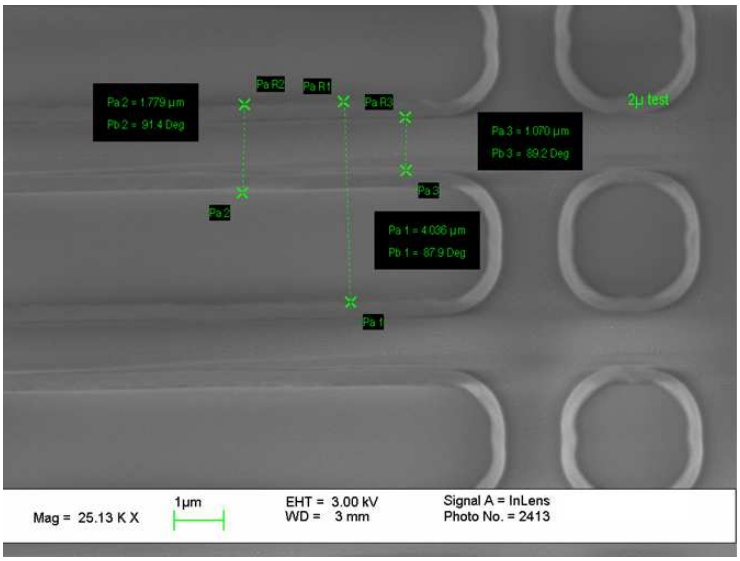

Figure 2.2: A SEM image of a typical test structure. On the mask the holes are square shaped, and the width of the waveguides is the same distance as the gap between them. The photolithography rounds corners as can be seen in the image. The width of the waveguides is 1.78 μm, and the gap between the waveguides is 2.22 μm. On the mask these values are both 2 μm, meaning that the line width reduction is 0.22 μm.

can either be deposited by plasma enhanced chemical vapor deposition (PECVD) or grown in a diffusion furnace. The advantage of fabricating the SiO_2 layer by PECVD is that the deposition rate is much higher than in the diffusion process; but growing the SiO_2 layer by diffusion gives much better uniformity, fewer defects, higher dielectric strength, better purity, batch processing, minimization of stress, and very high optical quality. For these reasons, thermally grown silicon dioxide is preferred for high-quality optical components.

The growth process requires clean silicon wafers to begin with, and up to 200 wafers can be grown in one run. The first step is to ramp up the temperature to the Si oxidation temperature of 1075 °C and bake the wafers to remove water and impurities. Then O_2 ($Si + O_2 \rightarrow SiO_2$) and deionized (DI) water vapor ($Si + H_2O \rightarrow SiO_2 + 2H_2$) from a quartz bubbler flows in to the furnace and the oxidation begins. The H_2O is added to speed up oxidation process. It takes about three weeks to grow a 12 μm thick layer, which is much slower than PECVD, where glass can be grown to the same thickness in less than an hour. But the quality is much higher and 200 wafers can be grown at the same time.

2.2 Chemical vapor deposition (CVD and LPCVD)

The following section is based on chapters 4, 5, and 7 in "The Materials Science of Thin Films" by M. Ohring [1].

Core layers for integrated optical components must satisfy a number of criteria: Good thickness and index uniformity across an entire wafer, reproducibility, very few particles (in order to have low scattering losses), low absorption losses, and low stress (to avoid birefringence and processing difficulties). Such layers can be deposited in many different ways, one of them being chemical vapor deposition (CVD).

CVD is a process in which one or more gaseous species enter the reactor from gas tanks or liquid bubbler sources outside the reactor. The reactants then combine at the hot substrate to produce a solid film. In order for the reaction to occur, the compound elements must exist in volatile form and be sufficiently reactive.

The large variety of materials that can be deposited by CVD methods have inspired design and construction of a many different processes and

systems. In order to distinguish them they are divided into categories according to such properties as temperature (low or high), pressure (atmospheric or low), and temperature (cold or hot). The number of potential CVD processes can be further expanded by the incorporation of physical deposition such as plasmas and evaporating sources.

The properties of the silicon nitride layers are strongly influenced by the processing conditions: Producing Si_3N_4 by the process:

$$3SiCl_2H_2(g) + 4NH_3(g) \rightarrow Si_3N_4(s) + 6H_2(g) + 6HCl(g) \tag{2.1}$$

at 750 °C gives an insulating and passive film. In contrast, the reaction:

$$3SiH_4 + 4NH_3(g) \rightarrow Si_3N_4(s) + 12H_2(g) \tag{2.2}$$

at 250 °C results in a porous thin film with considerable amounts of hydrogen incorporated. Hydrogen is generally undesirable in SRN thin films, because it bonds to nitrogen and produce N-H bonds, which leads to large absorption losses at telecommunication wavelengths.

Gas transport is a process by which volatile species flow from one part of a reactor to another. When designing a CVD process, it is important to understand the nature of the gas transport because:
a) The uniformity of the thickness of the deposited film depends on the delivery of equal amounts of reactants to all substrate surfaces;
b) High deposition growth rates depend on optimizing the flow of reactants through the system and onto the substrates;
c) A more efficient utilization of the process gases can be achieved.

A diffusion flow is a motion of individual atomic or molecular species. If two different gases are initially separated and then allowed to mix, each will move from regions of higher to lower concentration, thus increasing the entropy of the system (Fick's law [2]). The diffusion constant D varies inversely with pressure, i. e. reducing the pressure in the reactor can enhance the gas mass transfer rates. LPCVD utilizes this advantage.

Film growth is determined by viscous, diffusive, and convective mass transport fluxes that are driven by gas pressure gradients. In closed reactors these are caused by temperature differences that locally change the equilibrium partial pressures.

The deposition kinetics of CVD films depends on several factors associated with the gas-substrate interface, including:

a) Transport of reactants through the boundary layer to the substrate;
b) Adsorption of reactants at the surface;
c) Atomic and molecular surface diffusion, chemical reactions, and incorporation into the lattice; and
d) Transport of products away from the substrate through the boundary layer.

The microscopic details of these steps are usually not known, therefore one often models the system in macroscopic terms in order to predict deposition rates and uniformity within the reactors.

The actual film structure morphologies that develop during CVD are the result of a complex sequence of atomic migration events on substrates leading to observable nucleation and growth processes [3].

2.2.1 Low-pressure chemical vapor deposition (LPCVD)

Historically, LPCVD methods were first established to produce polysilicon films with a high degree of and control of stoichiometry and contamination problems. In principle it is possible to deposit large batches of wafers (∼100) at a time. This fact, and the generally high deposition rates, improved film thickness uniformity, improved step coverage, reduced particle density, and fewer pinhole defects gives LPCVD economic advantages compared to atmospheric CVD.

The gas pressure in LPCVD processes is typically 0.1 to 1 Torr (in atmospheric CVD it is around 760 Torr). In order to compensate for the low pressures, the input reactant gas concentration is correspondingly increased relative to a reactor at atmospheric pressure. Since the diffusivity varies inversely with the pressure, reducing the pressure may enhance the gas mass transfer rates. Low gas pressures generally enhance the mass flux of gaseous reactants and products through the boundary layer between the laminar gas stream and substrates. The increased mean free path of the gas molecules enables the substrates to be packed more closely, resulting in a higher throughput.

Commercial LPCVD systems (see figure 2.3, which shows the LPCVD setup in the cleanroom) are usually horizontal hot-wall reactors, which shows the LPCVD setup in the cleanroom). It consists of a cylindrical quartz tube heated by wire-compound elements, in which the substrate wafer stack is introduced on a "wafer boat" (see figure 2.4). Mass flow

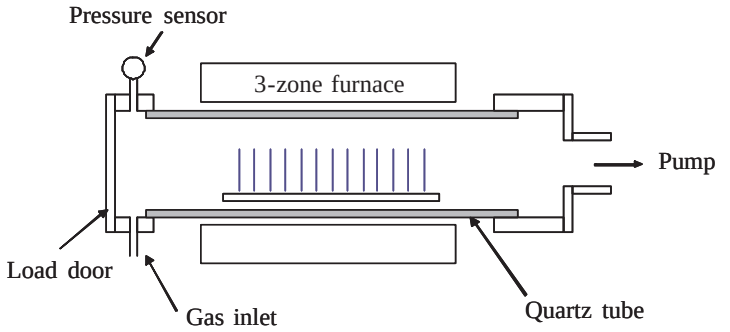

Figure 2.3: Overview of the LPCVD setup. A wafer boat (in blue) is placed inside the quartz tube. The tube is heated and kept under low pressure during deposition.

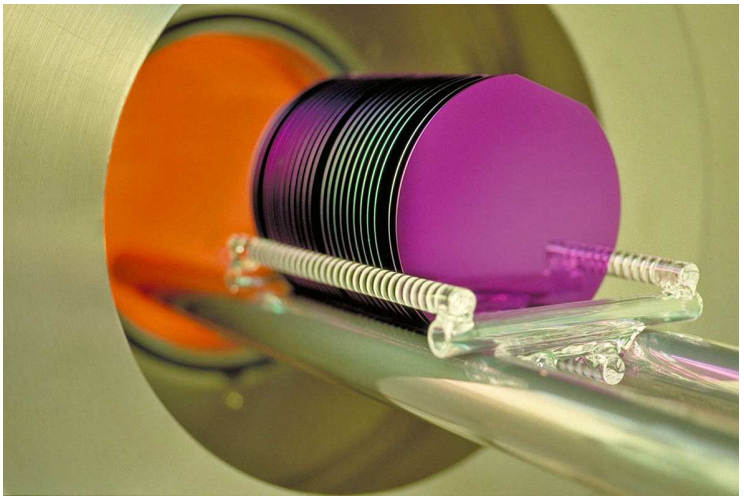

Figure 2.4: Picture of a batch of wafers in a boat entering the LPCVD furnace. Photo by Karsten Damstedt.

controllers (not shown in the figure) provide the required gas flows at the gas inlet, and large mechanical pumps maintain the required operating pressure.

As a starting point an existing recipe for silicon nitride was used where the temperature and pressure were constant. The gas flows were then varied until an optimum (with respect to index, thickness, uniformity, stress etc.) thin film for optical core layers was found.

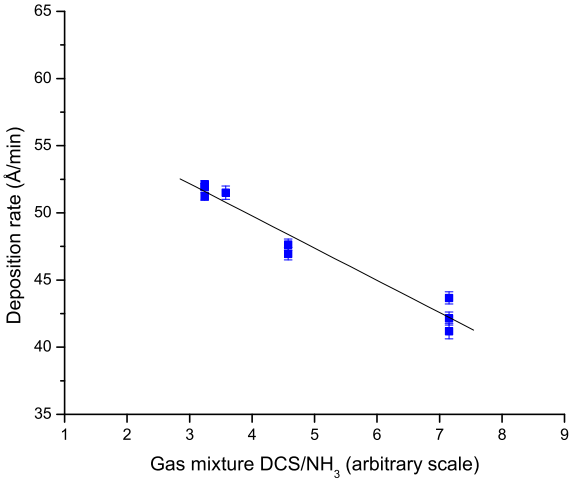

Figure 2.5: Deposition rate versus gas mixture averaged over 28 wafers from the same deposition run. The solid line is a guide to the eye.

The gases used for SRN deposition are NH_3 and DCS but it is also possible to deposit stoichiometric silicon nitride (Si_3N_4) which has a refractive index of 2.00 (at a wavelength of 1550 nm) and a thickness up to 1 μm. Using a range of deposition recipes gives a variety of SRN thin films with refractive indices varying from 1.9 to 2.3 (at a wavelength of 1550 nm) and thickness up to 1.5 μm [4]. SRN is preferred due to the higher refractive index and much lower stress than more Si poor films [5]. The optimum deposition rate as a function of gas mixture is illustrated in figure 2.5. An index variation of more than 10% can be obtained by varying the gas mixture; see figure 2.6. The symbols represent values obtained from different deposition runs. The trend of the results in figure 2.6 is in agreement with what can be found in the literature [6]. It can be seen from the figure that as the DCS/NH_3 ratio increases the refractive index increases, and by extrapolating the data to very large values of DCS/NH_3 the index increases to the value of that of pure silicon.

The surface roughness (root mean square) has been measured by atomic force microscopy (AFM) and has been found to be around 3 nm for annealed samples. This roughness is acceptable for high index low

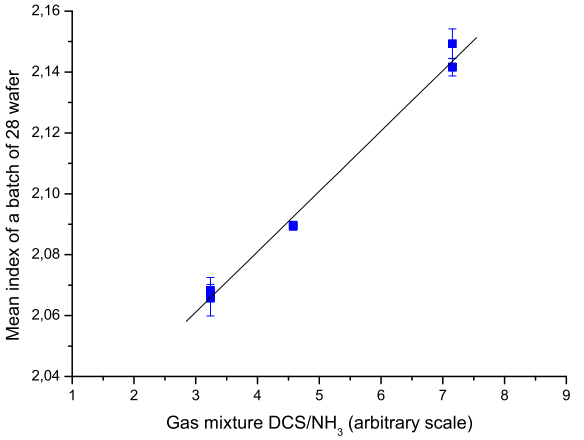

Figure 2.6: Refractive index measured at 633 nm versus gas mixture ratio averaged over 28 wafers from the same deposition run. The solid line is a guide to the eye.

.

loss optical waveguides operating at wavelengths in the telecommunication band (1530 - 1570 nm). This will be discussed in more detail in section 4.1.1).

Several identical production runs were made in order to test the reproducibility of the process. The yield was found to be of the order of 99%, both for the thickness and the index. The maximum variation in thickness from wafer to wafer across a whole boat of 28 wafers is 6.9% (see figure 2.7); across a single wafer it is only 1.7%. The maximum variation in refractive index across a boat of 28 wafers is 0.03%, and there is no systematic trend in the variations across each wafer.

This gives the LPCVD process yet another advantage over the PECVD process, in that calibration is not needed before each deposition run. The precision requirements on the thickness (to enable single mode operation of SRN waveguides) then allow using $12-14$ of the wafers from each run, about half of the total number. The uniformity of the refractive index is so high that the thickness variations alone determines the yield. This means that there will be a set of $12-14$ wafers from each run that can be considered identical and therefore can be used for very high quality com-

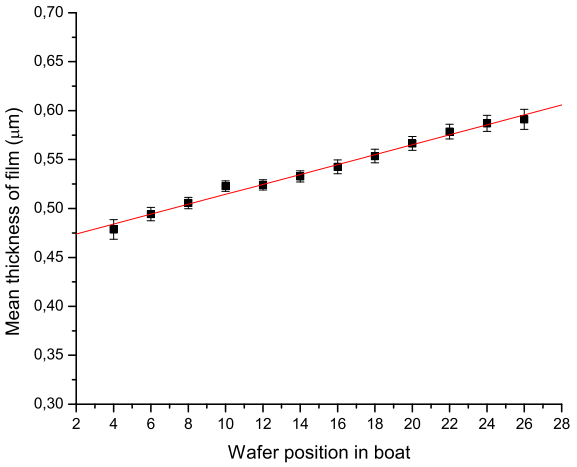

Figure 2.7: Mean thickness as a function of wafer position number in the deposition boat. The solid line is to guide the eye.

ponents. The remaining wafers are used to monitor the various process steps.

Stress, measured with profilometry and calculated using Stoneys equation[1] [7], ranged between 50 MPa tensile to 250 MPa compressive as function of gas mixture, giving a low bending of the wafer. It was observed that the stress was reduced when increasing the DCS flow. This is in agreement with expectations from the literature, see for example [6] or [8]. For the final optimized deposition process with an anneal of 1100 °C, the stress was very low, only 50 MPa tensile. This implies that waveguides can be made with negligible birefringence.

[1]

$$\sigma_f = \frac{Y_s d_s^2}{6 d_f} \left(\frac{1}{R_c} - \frac{1}{R_s} \right) \tag{2.3}$$

where σ_f is the film stress, Y_s is Young's modulus of the substrate, d_s is the thickness of the substrate, d_f is the thickness of the thin film, R_c is the radius of curvature of the composite (substrate + thin film), and R_s is the radius of curvature of the bare substrate.

2.3 Photolithography

Once the core layer has been examined and fulfills all the requirements, structures can be fabricated by photolithography in this layer. Photolithography involves transferring patterns from a predesigned high resolution mask onto a photosensitive film. This film can be used as an etch selective mask for transferring the patterns from the photosensitive film to the SRN core layer.

To achieve the best condition for photolithography it is crucial to first prepare the wafers to ensure good adhesion of the resist. The wafer is initially heated in an oven to a temperature sufficient to drive off any moisture that may be incorporated in the film surface. In our cleanroom we use a standard temperature of 150 °C. Hexa-methyl-disilizane (HMDS) is applied in vapor form in order to promote better adhesion of the photo-sensitive polymeric material, the photoresist.

A SSI 150 dual track spinning machine capable of making thin (below 100 nm) and thick (up to 10 μm) photoresist is used. Photoresist is dispensed in liquid form onto the wafer while the wafer is rotating. The speed and acceleration of this rotation are important parameters in determining the resulting thickness of the applied photoresist. The photoresist coated wafer is then transferred to a hot plate where a soft bake is applied; the purpose of this bake is to drive off excess solvent before insertion into the exposure system. A resist thickness of 1.5 μm is sufficient for 0.6 μm SRN due to the high etch selectivity with an optimized etching recipe.

The desired pattern is then projected onto the wafer in an aligner (Karl Süss MA/BA6). Here the light from a mercury arc lamp passes through the predesigned mask to produce the desired image on the wafer through a reduction lens system. When the image is projected onto the wafer, the photoresist material undergoes wavelength-specific radiation-sensitive chemical reactions, which cause the regions exposed to light to become either more or less acidic.

If the exposed regions become more acidic, the material is called a positive photoresist, while if it becomes less susceptible to the light it is a negative photoresist. The resist is then developed by exposing it to an alkaline solution such as sodium hydroxide, which removes either the exposed or unexposed photoresist. The exposure and developing times

must be adjusted to give structures of the desired size and without leaving excess or lack of resist. The resulting wafer is then post baked in order to solidify the remaining photoresist to serve as a protecting layer in the next step, the plasma etching.

The ability to produce a clear image of a very small feature onto the wafer is limited by the wavelength of the light that is used. Current state-of-the-art photolithography tools use e-beam writing where the feature size can be below 7 nm.

The aligner used in this work (see above) employs a 350 W Hg lamp, which radiates light from 275 to 450 nm with the main peaks around 365, 410 and 440 nm. There is an I-line filter that blocks either all light under 355 and over 380 nm or nearly all light under 365 nm. This corresponds to a maximum resolution of 0.7 μm. During exposure it is necessary to use contact exposure mode between the mask and the photoresist on the wafer since 0.6 μm structures are just at the resolution limit of the system.

2.4 Reactive ion etching (RIE)

After the pattern from the predesigned mask has been successfully transferred onto the photoresist, a selective etch is used. This etch is required to etch through the SRN layer before all the photoresist is etched away if the structures are to be transferred onto the SRN layer. This is the goal for the combined photolithography and etching processing steps. Having complete control of the lithography and etching enables one to make masks with a high degree of tolerance and a high yield of components on each wafer and in each processing batch.

Etching of microstructures can be done in many ways [9]. There are two basic techniques, dry and wet etching. Dry etching has a variety of advantages compared to wet etching including: more anisotropic etching, fewer disposal problems, less corrosion of metal features, better critical dimension control, and cleaner resulting surface under the right circumstances.

A dry etch is typically a plasma etching i.e. etching in a glow discharge. The plasma is generated in a vacuum chamber where the substrate is located, and physical and chemical processes occur. Impacting ions, and electrons either induce chemical reactions or, in sidewall-protected ion-assisted etching, a passivation layer for integrated circuits is cleared by

the particle bombardment from horizontal surfaces only. As a result, etching occurs mostly on the cleared plane surfaces.

It is important to design the etch process to have high selectivity between the mask and thin film; i.e. the mask must be etched much more slowly than the thin film. The degree of anisotropy and selectivity is controlled by the plasma conditions. At low pressures (mTorr), etching is anisotropic due to sputtering but the selectivity is poor. At higher pressures (1 Torr), chemical effects dominate and lead to better selectivity at the cost of turning the process isotropic.

Finding the perfect etching conditions amounts to finding the right balance between physical and chemical etching processes. The physical etch is a physical ion bombardment and inherently anisotropic, while the chemical etch is a chemical reaction with a reactive species at the surface, and thus more isotropic. For waveguides, the goal is a completely anisotropic etch to be able to control the sidewall angle and a low sidewall roughness.

The system available is a STS reactive ion etching (RIE) chamber. The RIE chamber has a monochromator attached for end point detection. The monochromator monitors the material being sputtered away from the surface of the wafer, and thereby allows to stop the etch when the core layer has been etched through. The parameters which can be varied are gas flow and mixtures: CF_4, CHF_3, SF_6, O_2, C_2F_6, N_2, Ar, H_2, power and pressure. While optimizing the etch, the power, pressure, and gas flows are varied in order to find a combination of gases yielding the best balance between chemical reactions and physical sputtering of the thin film to yield smooth 90° sidewalls.

Initially, an existing silicon etching recipe was used because the SRN thin films are silicon rich. Silicon etching by fluorine is a purely chemical process, so there is no need for ion bombardment [10]. The most widely used gas mixtures for RIE of silicon contain fluorine, chlorine, oxygen and carbon: C_2F_6 and O_2, SF_6 and CF_4. Those most commonly used in our cleanroom are SF_6 and CF_4. CHF_3, which is usually used to etch silicon dioxide, can also be used as a silicon etchant. The gas molecules are dissociated in the RF plasma, producing primarily free atomic fluorine (F), molecular fluorine (F_2), atomic hydrogen (H), some unsaturated species based on CF_2 (CF_x), and fluorine sulphur radicals as well [11].

The latter dissociation products tend to form polymers on surfaces

[10]. The presence of hydrogen in the plasma facilitates the formation of fluorocarbon polymers, especially in plasma chemistry comprising CHF_3 and CF_4. At sufficiently high CHF_3 flows the formation of polymers will more than compensate for the removal caused by the plasma etch, and the etch rate will be reduced to zero; this is called the polymer point. However, the polymers can be removed by adding oxygen (O_2) to the plasma.

In the literature (see for example [12–15]), etching of silicon nitride has been performed with both wet etch (for example H_3PO_4 [16]) and dry etching. However, most of the numerous articles describe the SRN as a masking material rather than as a thin film for components (see for example [13], which uses CF_4 and O_2 for etching, [14] which uses CHF_3 and O_2 for etching, or [15] which uses C_2F_6). Some articles have focused on anisotropy, but they have all had the goal of producing other structures, for example grooves, rather than waveguides with smooth 90 ° sidewalls.

The first experiment with the silicon etching resulted in large sidewall roughness and increased angle of the side walls (see figure 2.8). The gas combinations, power, and pressure were then varied in order to optimize the process and make it more physical, hereby producing 90° sidewalls. An optimized glass (Ge:SiO_2) etch was also tried, but it turned out to give increased side wall angles as well.

In the end, the optimal SRN waveguide (see figure 2.9) etch was found to be a combination of the silicon and silica etch (in agreement with Schaepkens et al. [17]). It consists of three steps: The first step is a surface cleaning processes, which includes a short polymer etch. This etch basically involves oxygen and nitrogen at relatively high pressure and medium applied power. The purpose of this step is to remove any residual resist on the surface, which often remain after developing. The waveguides are almost unaffected by this etch, but any residual polymer is completely removed. The next step is the SRN etch, and the last etching step is resist removal in an oxygen plasma.

After multiple experiments, it turned out that C_2F_6 and CHF_3 in the ratio of 2:1 were the best gasses for an ideal combination of chemical and physical etching of SRN. Also low power (< 100W) and low pressure (< 200 mTorr) resulted in a good selectivity, smooth side walls and 90° sidewall angles. The selectivity is the rate at which one material is etched

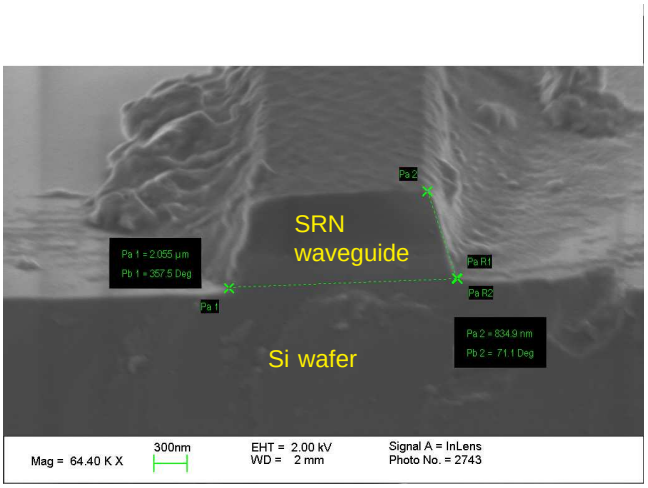

Figure 2.8: A cross section SEM image of the first etching attempt. The inspected wafer is a test wafer with no thermal oxide and top cladding. The side walls are not close to 90° and they are very rough.

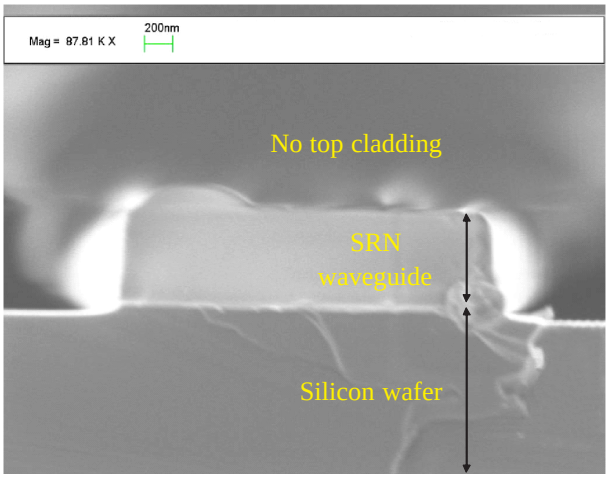

Figure 2.9: A cross section SEM image of the optimal etch. The inspected wafer is a test wafer with no thermal oxide and top cladding. The angle of the side walls is very close to 90°.

relative to another. A selectivity of 1:3 photoresist:SRN thus means that 0.2 μm of photoresist etched for every 0.6 μm SRN etched.

The etch rate and sidewall angles were determined by examining cross sections and tilted samples (wafer, thermal oxide, and SRN waveguides) in a SEM and were found to be 35.3 nm/s and 90° (see figure 2.9) respectively. However, the sidewall angle was chosen to be a little less than 90° (87°) in order to ensure good step coverage of the top cladding. The line width reduction was also determined by examining test structures, like the one seen in figure 2.2, in the SEM. The waveguide width and separation were the same on the mask; after etching the waveguides were narrower. The line width reduction was measured using SEM to be 0.3 $\pm$ 0.1 μm.

2.5 Top cladding

Different types of glass can be used as top cladding for optical waveguides. One very commonly used glass is boron and phosphorous doped silica glass (BPSG), a soft glass which is deposited by PECVD. BPSG is an SiO_2 matrix with P_2O_5 and B_2O_3. The refractive index is between 1.445 and 1.449 measured at 633 nm, and it can be varied by adjusting the P (increases the index and makes the glass soft) and B (reduces the index) flow rates.

When annealed at around 1000 °C, the glass will flow, densify, and cover the SRN structures. Annealing of the top cladding is performed in a water vapor atmosphere, which also helps to oxidize and smoothen the soft glass surface. Soft glass makes it possible to cover the waveguide structures completely and avoid pinholes and trenches in the corners between the waveguides and the thermal oxide.

The refractive index of the annealed top cladding is index matched to the thermal oxide underneath the SRN structures. The annealing procedure has been optimized so as to minimize the stress in the total system (wafer, thermal oxide, SRN waveguide structures, and top cladding).

2.6 Conclusions

A stable fabrication technique for processing of reproducible low stress SRN thin films and waveguides with an excellent uniformity in thickness

and index has been developed. The index of the films can be tuned by altering the gas flow ratio of the gasses used in the deposition process. In the literature index steps (between the SRN core and the silica cladding) varying from $\Delta n = 0.5$ to 1.3 have been demonstrated [4]. Stress effects in optical components are a major issue; the mechanical stress causes birefringence, which yields large polarization dependent loss. In SRN films the stress was reduced to around 50 MPa through deposition and annealing optimization. For comparison stress ≤ 10 MPa has been reported [4]. Using SRN for optical components, the stress induced birefringence can thus be neglected. The critical step in the processing of waveguides (besides thin film uniformity and particles), photolithography and RIE etching has been optimized in such a way that it is possible to fabricate 0.6 μm wide structures with UV-photolithography. This is a difficult task since the wavelength of the light during exposure limits the resolution of feature sizes. The surface and sidewall roughnesses have also been investigated, and they both are within the limits of what is acceptable for making low loss waveguides (this will be discussed further in section 5.4.1).

Chapter 2 references

[1] M. Ohring. *The Materials Science of Thin Films*. Academic Press, Inc., 1992. ISBN 0-12-524990-X.

[2] N. W. Ashcroft and N. D. Mermin. *Solid State Physics*. Harcort Brace College Publishers, International edition, 1976. ISBN 0-03-049346-3.

[3] J. Bloem and W. A. P. Claassen. "Nucleation and growth of silicon films by chemical vapour deposition", *Philips Technical Review*, vol. 41, no. 2, pp. 60–9, 1983.

[4] M.-C. Cheng, C.-P. Chang, W.-S. Huang, and R.-S. Huang. "Ultralow-stress silicon-rich nitride films for microstructure fabrication", *Sensors and Materials*, vol. 11, no. 6, pp. 349–58, 1999.

[5] R. Pandey, L. Patil, J. Bange, and D. Gautam. "Growth and characterization of silicon nitride films for optoelectronics applications", *Optical Materials*, vol. 27, no. 2, pp. 139–146, 2004.

[6] M. Sekimoto, H. Yoshihara, and T. Ohkubo. "Silicon nitride single-layer X-ray mask", *Journal of Vacuum Science and Technology*, vol. 21, no. 4, pp. 1017–21, 1982.

[7] G. Stoney. "The tension of metallic films deposited by electrolysis", *Proceedings of the Royal Society of London. Series A, Containing Papers of a Mathematical and Physical Character*, vol. 82, no. 553, pp. 172–175, 1909.

[8] K. E. Bean, P. S. Gleim, and R. L. Yeakley. *Journal of Electrochemical Society*, vol. 114, p. 733, 1967.

[9] M. Madou. *Fundamentals of Microfabrication*. CRC Press LLC, 1997. ISBN 0-8493-9451-1.

[10] C. Laurent-Lund. *Multilevel integration of Optical Waveguides*. Ph.d. thesis, MIC, DTU, Denmark, august 1997. ISBN 87-89935-10-1.

[11] D. M. Manos and D. L. Flamm. *Plasma etching: An Introduction*, vol. 1. Academic Press, Inc., 1989. ISBN 0124693709.

[12] B. M. Dries. "Yield enhancement through defect reduction for post wet silicon nitride etch applications", *Advanced Semiconductor Manufacturing, 2004. ASMC '04. IEEE Conference and Workshop*, pp. 10–14, 2004.

[13] R. Knizikevicius, A. Galdikas, and A. Grigonis. "Real dimensional simulation of anisotropic etching of silicon in CF_4+O_2 plasma", *Vacuum*, vol. 66, no. 1, pp. 39–47, 2002.

[14] H. J. Stocker. "Selective reactive ion etching of silicon nitride on oxide in a multifacet ('HEX') plasma etching machine", *Journal of Vacuum Science & Technology A (Vacuum, Surfaces, and Films)*, vol. 7, no. 31, pp. 1145–9, 1989.

[15] A. Midha, S. K. Murad, and J. M. R. Weaver. "Anisotropic pattern transfer of fine resist features to silicon nitride via an intermediate titanium layer", *Microelectronic Engineering*, vol. 35, no. 1-4, pp. 99–102, 1997.

[16] C. Willis. "Nitride strip: Phosphoric acid bath-life above 100 hours", *Diffusion and Defect Data Pt. B: Solid State Phenomena*, vol. 65-66, pp. 127–130, 1999.

[17] M. Schaepkens, T. E. F. M. Standaert, N. R. Rueger, P. G. M. Sebel, G. S. Oehrlein, and J. M. Cook. "Study of the SiO_2-to-Si_3N_4 etch selectivity mechanism in inductively coupled fluorocarbon plasmas and a comparison with the SiO_2-to-Si mechanism", *Journal of Vacuum Science & Technology A (Vacuum, Surfaces, and Films)*, vol. 17, no. 1, pp. 26–37, 1999.

Chapter 3

Material Characterization of Thin Films

As described in chapter 2, Silicon Rich Nitride (SRN), deposited by LPCVD, is a low stress amorphous material with a high refractive index. After deposition the SRN thin film is annealed at temperatures above 1100 °C to break N-H bonds, which have absorption peaks in a wavelength band important for optical telecommunication (1530-1570 nm). However, silicon clustering appears in the thin films when annealing above 1150 °C. Clustering is undesirable in waveguide materials because the localized variations of the refractive index associated with the clusters lead to Rayleigh scattering, which can cause significant propagation loss in optical waveguides. Thus, the annealing temperature must be high enough to break the N-H bonds, but lower than the cluster threshold temperature. Therefore, the process window for the annealing step lies in the narrow window between 1100 °C and 1150 °C.

The chemical composition of amorphous silicon rich nitride has been investigated by synchrotron radiation, Rutherford Back Scattering (RBS), X-ray Photo-electron Spectroscopy (XPS), and spectral ellipsometry. The influence of deposition parameters and annealing temperatures on the stoichiometry and the chemical bonds will be discussed in the following sections.

By varying the ratio between the two deposition gasses, DCS and NH_3, it is possible to tune the refractive index from less than that of stoichiometric silicon nitride (Si_3N_4 with n = 2.0 measured at 633 nm) all

the way to that of silicon (n = 3.5 measured at 633 nm) [1]. Stoichiometric silicon nitride can exist in one of two chemical phases, α - Si_3N_4 and β - Si_3N_4 [2]. It is believed that the amorphous silicon rich nitride consists of separated stoichiometric Si_3N_4 and Si phases [3]. Furthermore it has recently been reported that there are different chemical phases in Si_xN_y corresponding to SiN_4, SiN_3Si, SiN_2Si_2, $SiNSi_3$ and SiN_4 tetrahedra [4]. The existence of silicon clusters in SRN has also been reported [5]. Which effects the clustering and various phases have on the optical properties have not, to the authors knowledge, been investigated yet.

3.1 Analysis methods

3.1.1 Synchrotron radiation

The crystallographic structure, possible preferred orientation of the crystals, and lattice constants and geometry of the films can be determined by using a variety of techniques; e.g. X-ray diffraction, synchrotron radiation, and X-ray photoelectron spectroscopy (XPS). Synchrotron radiation has been used, e.g. by H. Toraya, in work on the crystal structure refinement of α - Si_3N_4 [6].

In this work, synchrotron radiation has been used at HASYLAB (Hamburger Synchrotronstrahlungslabor) at DESY (Deutsches Elektronen-Synchrotron) in Hamburg to analyze two types of SRN films: one annealed at 1150 °C and one unannealed.

When analyzing SRN films with synchrotron radiation, one observes peaks in the measured spectra from both triagonal-Si_3N_4, from Si, from an amorphous background, and from the $< 100 >$ Si substrate (see figure 3.1). A clear difference between the annealed and the unannealed sample was observed: In the annealed samples there were more peaks for crystalline phases.

This result was obtained by analyzing the Si_3N_4 features, but the amorphous background has not been investigated. It is important to investigate also this background in order to gain further information about the SRN films. Such a study was initiated, but unfortunately difficulties with the software needed for the analysis were encountered. Therefore, further investigation of the chemical composition of SRN has been done using XPS.

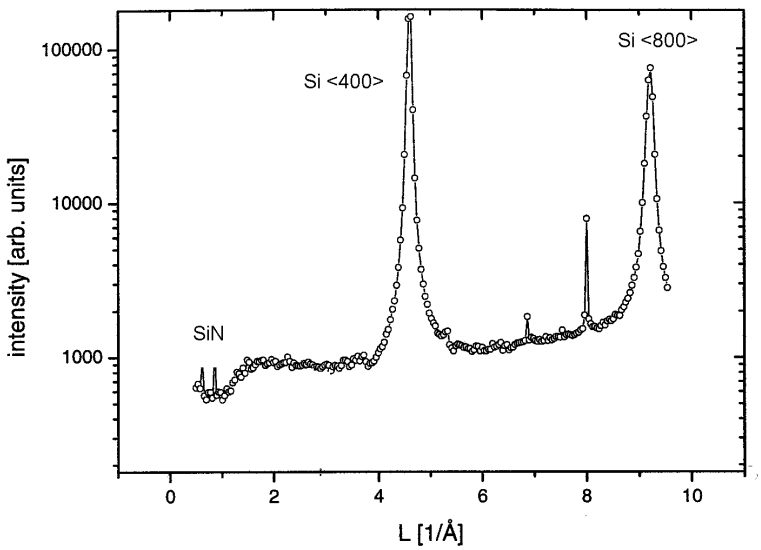

Figure 3.1: .
X-ray spectrum, intensity versus energy (in $Å^{-1}$)), of SRN on Si annealed at 1150 °C. Peaks from Si, triagonal-Si_3N_4, an amorphous background, and the $< 100 >$ substrate are present.

3.1.2 Rutherford Backscattering Spectroscopy (RBS)

Rutherford Backscattering Spectroscopy (RBS) is in principle the analysis of backscattered monoenergetic light ions, for example 2 MeV He ions, which are accelerated towards a sample. A very small portion of these ions will undergo collisions with the nuclei of sample atoms on the surface as well as in-depth and backscattered. The Rutherford forward scattering process can be represented as a simple two-body collision. This scattering event is so rare that the attenuation of the beam intensity on its path into the target is insignificant and the effect is usually ignored. The backscattered particles will however escape the sample and can be energy-analyzed. The backscattering energy distribution of the particles carries information on the mass and depth distribution of the sample atoms where scattering occurs, hence information on the depth profile of the sample.

RBS involves measuring the number and energy of ions in a beam which backscatter after colliding with atoms in a sample at which the beam has been targeted. With this information it is possible to determine atomic mass and elemental concentrations versus depth below the surface. The energy measured for a particle backscattering at a given angle depends upon two processes. Particles lose energy while they pass through the sample, both before and after a collision. The amount of energy lost is dependent on the material stopping power. A particle will also lose energy as the result of the collision itself. The collision loss depends on the masses of the projectile and the target atoms. The number of backscattering events which occur from a given element in a sample depends upon two factors: the concentration of the element and the effective size of its nucleus. A more detailed description of RBS is given in Appendix A.

RBS is the only technique for determining stoichiometry that is quantitatively precise to within a few at% without composition standards (when measuring concentration versus depth) for calibration [7]. It is also a non-destructive technique that samples the total thin film thickness (several μm) and parts of the substrate as well, depending on the stopping power of the matrix material. There are good detection limits for heavy impurities in light matrices. RBS also has the ability to measure the atom density of thin films when the thickness is known. The elemental sensitivity is from He to U, and it is only restricted by the

overlap between spectra of certain elements. It is possible to measure the stoichiometry and thickness of many composite layers, the dopant concentration in materials, and to detect metal impurities.

The RBS equipment at Institut für Physik at Universität der Bundeswehr München, Germany consists of a Van-de-Graaff linear accelerator with an energy range from 0.5 MV to 2.5 MV, a RF ion source, and a 30° magnet for mass and energy separation. The measurements were carried out with 1.8 MeV $4He^+$ ions. The SRN thin films were 500 to 650 nm thick, meaning that the RBS measurements probed both the thin films and the underlying substrate since the penetration depth of the ions was several microns. The acquired spectra were analyzed by the RUMP and SIM simulation programs [8].

3.1.3 X-ray photoelectron spectroscopy (XPS)

XPS yields information about the nature of the chemical bonds and valence states. Only the surface composition is determined; however, it is possible to probe deeper by sputter etching the thin film and continuously analyzing the exposed area. The elemental sensitivity goes from Li to U, and the detection limit is around 0.1-1 at% [**?**]. The lateral resolution is about 30 mm, and the effective probe depth is of the order of 3 nm.

The XPS setup used is located at Institut für Physik at Universität der Bundeswehr München, Germany. It is a commercial Omicron XPS system (see figure 3.2), consisting of a DAR 400 X-ray source, an EA 125 electron analyzer, and anodes of Al Kα emitting at 1486.92 eV, or Mg Kα emitting at 1253.6 eV. The line width and resolution are better with Mg as the anode material than with Al, but the Al anode is preferred for high-energy spectroscopy.

Argon ion sputtering equipment attached to the setup allowed depth analysis. The XPS chamber was then backfilled with high purity argon to a pressure of $1{\cdot}10^{-5}$ mbar and a 2 kV Ar ion beam were used for sputtering the sample. The sputter etch rate for SRN was found to be only 4 nm/hour, making depth profiling a very time consuming experiment. The result of an XPS measurement is a spectrum of intensity vs. binding energy for the surface layer material. Each compound in the layer emits one or more characteristic spectral lines, broadened into peaks by the instrumental resolution and superimposed on a continuous background

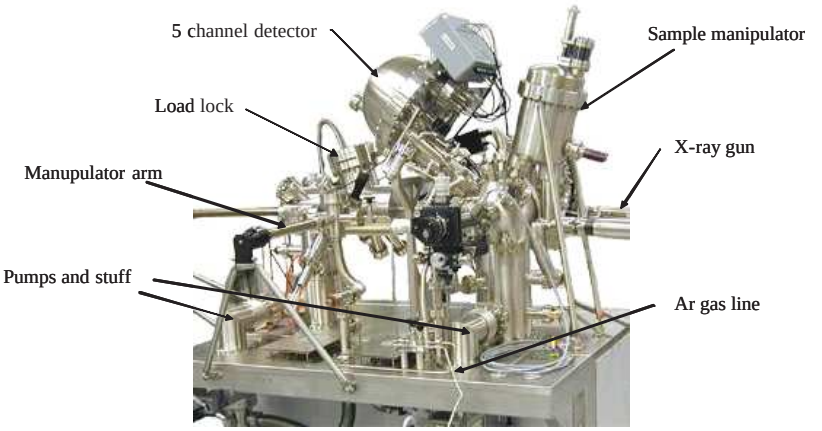

Figure 3.2: A picture of the XPS instrumental setup, from www.omicron.de. The instrument has a load lock system for transferring the sample into the UHV analysis chamber. The setup is equipped with an x-ray gun for analysis and an argon sputtering system for depth profiling.

signal. After proper background subtraction and sensitivity (cross section) calibration, the peak area of the lines is a quantitative measure of the concentration of the corresponding compounds. A more detailed description of XPS is given in Appendix B.

A commercial software, PRESENTS developed by Omicron, was used to fit the XPS spectra and to derive compound concentrations. The background subtracted from the spectral peaks was chosen to be a Shirley type [9], which removes the background iteratively. This is also the technique most commonly used for Si_3N_4 measurements [10].

Obtaining quantitative results for the specific element responsible for each peak requires knowledge of the elemental sensitivity, which is stored as a database in the program. The best estimate of the true composition of the sample is obtained by converting the relative peak areas (line equivalent widths) into percentages of a defined total mass, accounting for the relative sensitivities (cross sections) of the various peaks. Use of a curve fitting function in the spectral analysis is necessary in order to compute the peak areas and to deconvolute overlapping peaks (blended lines).

3.1.4 Spectral ellipsometry

Spectral ellipsometry is a powerful non-contact, non-destructive optical technique that enables determination of material refractive indices and layer thicknesses of a wide variety of materials in multiple layer film stacks. The technique is based on measurements of the change in polarization of a probing light beam upon reflection from a sample (see figure 3.3). When linearly polarized light reflects from a surface, elliptically polarized light is generated under certain conditions. The amount of induced ellipticity depends on the surface properties (refractive index, bulk, or layered sample). The phase and amplitude relationships between two orthogonal polarizations (p and s waves) upon reflection are measured. When p and s waves are reflected they experience a phase shift and an amplitude reduction. The ellipsometric parameter Δ is defined as d_1 - d_2, where d_1 and d_2 denote the induced phase shift differences between p and s waves, respectively, while the ellipsometric parameter $\tan(\Psi)$ is defined as the ratio of the complex amplitudes of the total reflection coefficients of the p and s waves. The ellipsometric parameters, amplitude ratio and phase change, are measured over a broad wavelength range. The parameters of interest to the process engineer, thickness and refractive index as a function of wavelength, are calculated from the measured amplitude ratio and phase changes using a regression process [11]. The regression compares the measured spectra with values calculated from initial estimates of the film parameters.

The ellipsometer used, at Institut für Physik at Universitüt der Bundeswehr München, Germany, was a Sopra ES-5 Spectral ellipsometer covering the wavelength range 190 - 800 nm.

3.2 Results of the measurements

3.2.1 Rutherford Backscattering results

With RBS, the stoichiometry of the thin films was measured for several combinations of gas flow and annealing temperature. Typical spectra of unannealed and annealed SRN thin films are shown in figure 3.4. In the spectrum illustrated below, the silicon peak has a step at its high-energy end: the lower peak is the SiN; the higher peak is the silicon wafer. It can be seen that the measured and simulated spectra are in good agreement.

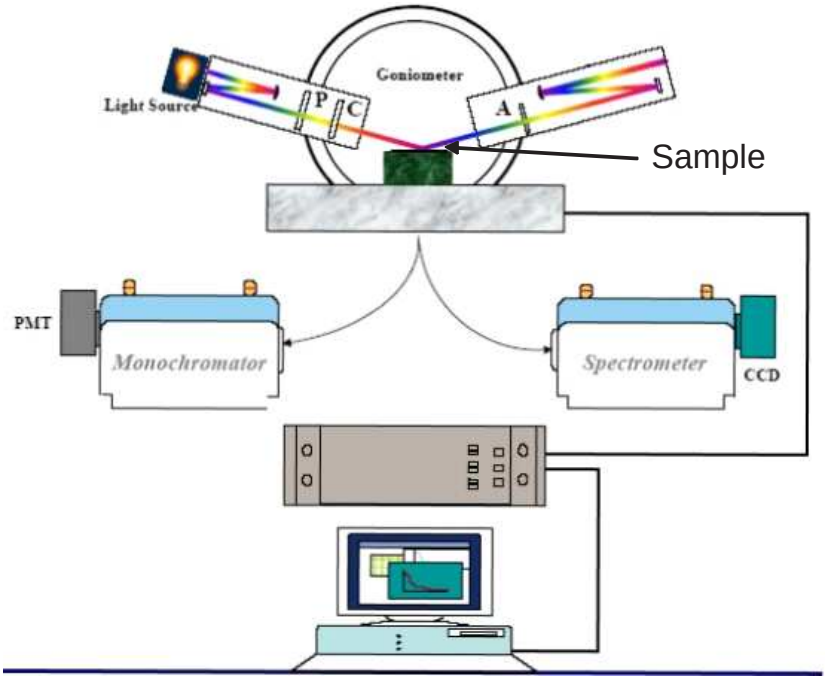

Figure 3.3: Spectral ellipsometry setup [mit-pbg.mit.edu/Pages/Ellipsometry.html]. The technique is based on measurements of the change in polarization of a probing light beam upon reflection from a sample.

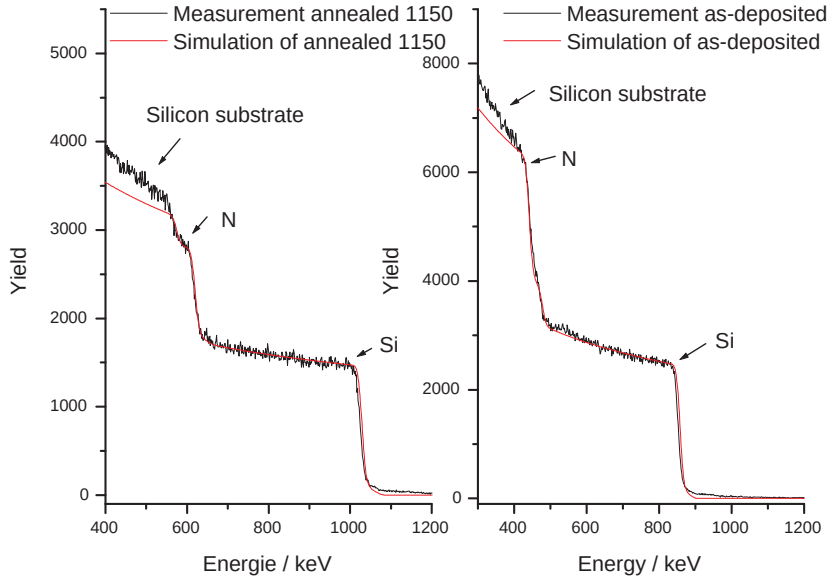

Figure 3.4: Typical RBS spectra of an annealed and as-deposited SRN films. The black curves are the measured data, and the red curves are the simulated spectrum.

The deviation of simulated contra measured spectra at low energies is due to multiple scattering. Before annealing the stoichiometry (x in SiN_x) was 0.91 and after annealing it was 0.64. This change in the stoichiometry means that the films become more silicon rich.

RBS measurements have shown that an increase of the DCS/NH_3 flow ratio causes an increase in the silicon concentration in the thin films (figure 3.5), as expected from the literature (see for example [12]). The refractive index also increases with higher DCS/NH_3 flow ratio [1] due to the higher silicon concentration [13], [14] and [15]. The refractive index for stoichiometric silicon nitride is 2; for pure silicon it is 3.5. This means that as the silicon concentration in the SRN increases, the refractive index changes from the value of Si_3N_4 to that of Si.

When annealing the thin films they tend to shrink one to two percent in thickness due to out-diffusion of residual gases and the refractive index

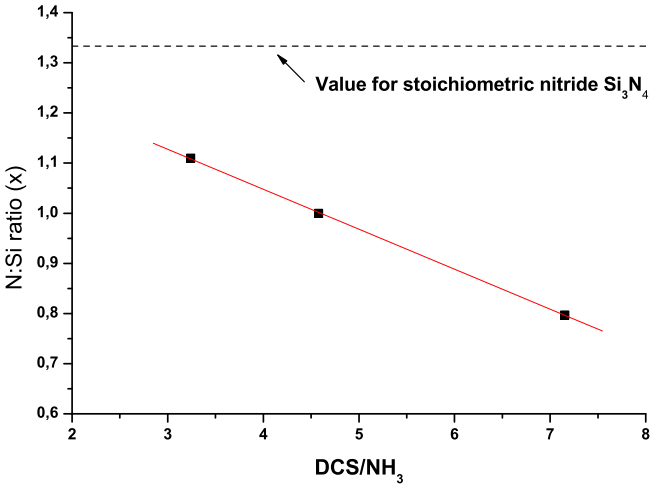

Figure 3.5: SiN_x as a function of the DCS/NH_3 flow ratio for unannealed thin films measured by RBS. The solid line is a linear fit; the dotted line indicates the composition of stoichiometric silicon nitride.

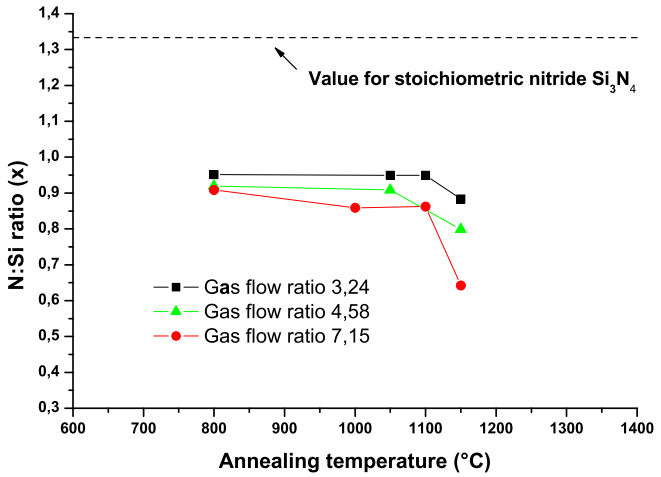

Figure 3.6: SiN_x as a function of annealing temperature for various DCS/NH_3 deposition mixtures measured by RBS. The dotted line indicates the composition of the stoichiometric nitride.

increases slightly (0.05 %) when annealing at temperatures over 1100 °C. RBS measurements show that the silicon concentration increases for samples annealed above 1100 °C (see figure 3.6). This result was quite surprising at first. The increase in refractive index is in good agreement with the higher silicon content, but where the excess silicon comes from was not obvious at first. The explanation for these results was found by the XPS experiments, which are discussed in the next section.

3.2.2 X-ray photoelectron spectroscopy results: SRN on Si substrate

XPS measurements were performed on 34 nm thin films deposited with various gas flows and annealed at temperatures ranging from 800 to 1150 °C. The thickness of the thin films was chosen such that the sputtering time from the surface to the interface between the thin film and the silicon substrate would be reasonable. Sputtering of the thin films was done in order to detect possible changes in stoichiometry and chemical

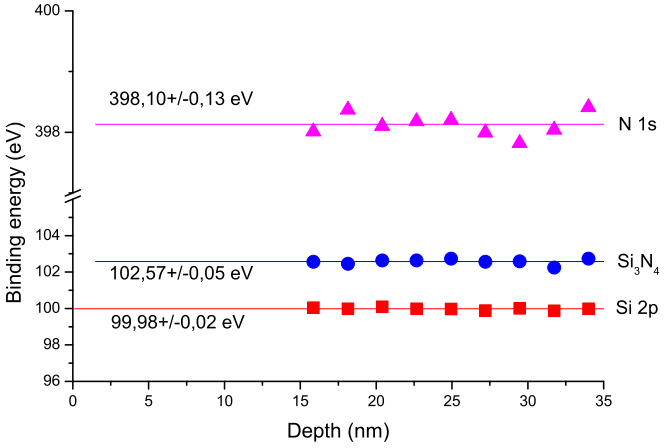

Figure 3.7: Binding energies of the Si2p (pure silicon; squares), N1s (triangles), and Si2p (SiN_x) (circles) peaks, as measured by XPS, as a function of depth in a 34 nm SRN film on a Si substrate annealed at 1150 °C. The solid lines show the fitted mean values. The gas ratio for deposition, DCS/NH_3, is 3.24.

composition throughout the thin film.

The binding energies of the N, Si, and Si_3N_4 were constant; the values vary only a few percent throughout the thin films. This was observed for all samples, annealed as well as unannealed. This implies that all the investigated thin films have the same types of chemical bonds, and that they remain the same throughout the thin films. An example is shown in figure 3.7. The measured binding energies are in agreement with data for SiN_x from standard XPS databases (see for example NIST SRD 20 Database of XPS Binding Energies or [4]).

Also, the stoichiometry shows no change throughout the unannealed films (see figure 3.8). At the surface and interface between the SRN thin film and the substrate, carbon and oxygen contamination is also present, because the samples have been handled in air.

The stoichiometry of the samples as measured by XPS does not quite match that derived from the RBS measurements, but the same dependence on the temperature (compare figure 3.6 and 3.9) and gas flow ratio is seen as with RBS. This is because RBS is the only technique that is

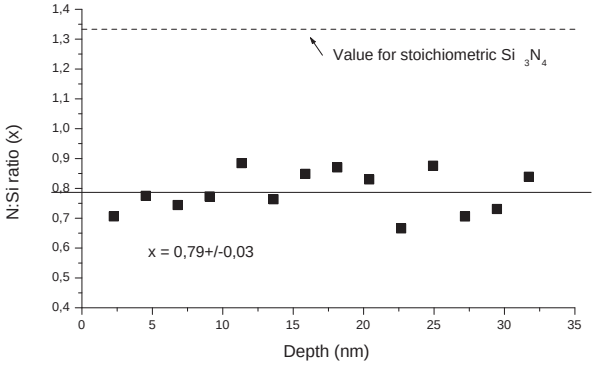

Figure 3.8: Depth profile of the stoichiometry of an unannealed SRN thin film on a Si substrate, as measured by XPS. The solid straight line is a linear fit; the dashed line indicates the composition of stoichiometric Si_3N_4. The DCS/NH_3 flow ratio is as in figure 3.7.

quantitatively precise at the atomic percent level without composition standards, while XPS is a more qualitative method.

There is a distinct difference between the spectra of unannealed film and samples annealed at 1100 °C and 1150 °C indicating that structural changes occur during annealing. A typical spectrum of an annealed sample is shown in figure 3.10. The areas of the N1s and Si_3N_4 peaks have been fitted, and the stoichiometry is found by using the respective sensitivity factors for the compounds. A zoom in on the Si and Si_3N_4 peaks and the corresponding fitted curves is also shown in figure 3.10. It can be seen that the area under the peaks fit the measured spectrum very nicely. High-resolution scans were performed in order to resolve the relative contributions of the Si-Si bonds and Si-N bonds to the Si2p peak around 99-102 eV, which is very difficult to resolve when either the pure Si or the SiN_x fractions are small. These measurements refer to the average composition through the film. In order to trace their origin more closely, a high-resolution scan of the two silicon compound peaks in the annealed sample (T=1150 °C) as a function of depth in the film was made; it is presented in figure 3.11. It is seen that the Si2p peak derived from Si_3N_4 decreases through the sample, while the percentage of pure Si increases at the same time. At the surface the composition is mostly Si_3N_4, while

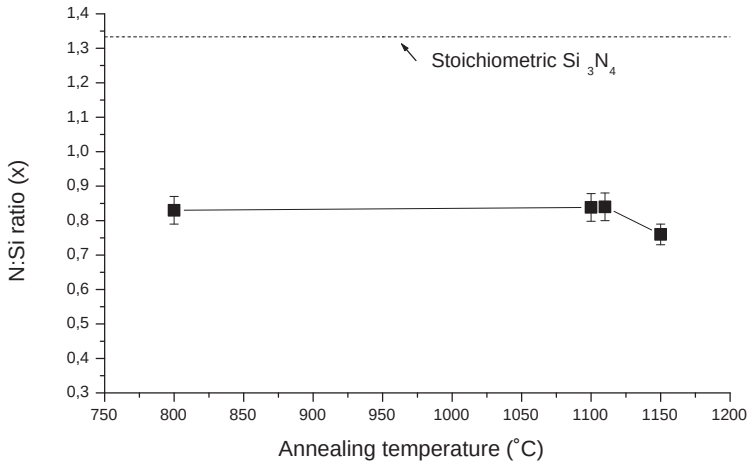

Figure 3.9: The average stoichiometry, SiN_x, through a thin film on Si substrate as a function of annealing temperature, as measured by XPS. The dotted line indicates the value of stoichiometric silicon nitride. The DCS/NH_3 flow ratio was 3.24.

at the interface between the film and the substrate it is free Si.

The amount of silicon in the samples increases with the DCS/NH_3 gas flow ratio. The amount of free silicon also increases with annealing temperature above 1100 °C (see figure 3.9). It can be seem in the figure that the stoichiometry is constant for temperatures up to 1100 °C whereafter the amount of silicon increases. The same tendency was seen by RBS measurements (figure 3.6).

When performing depth profiling there appears to be an intermediate layer with higher concentration of free Si between the SRN thin film and the substrate. As can be seen in figure 3.12 there is a concentration gradient of silicon in films annealed at 1150 °C but not in the as-deposited samples. This intermediate layer is less developed at lower annealing temperatures, but increases drastically in thickness, extending all the way to the surface of the SRN film, for annealing temperatures above 1110 °C. These results indicate that there is diffusion of silicon from the substrate into the thin film, and that this diffusion becomes more and more pronounced for high temperatures (above ∼1100 °C).

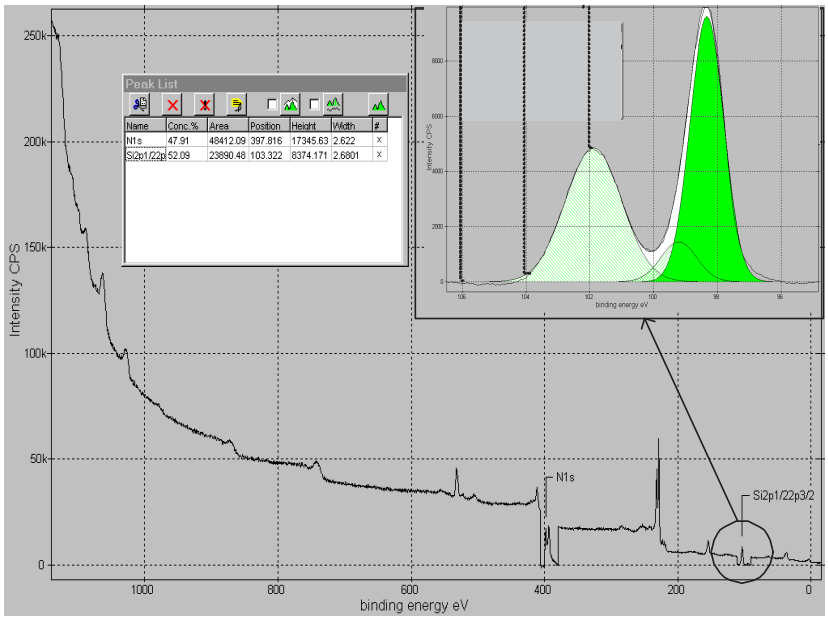

Figure 3.10: A typical XPS spectrum of an annealed sample. The areas of the N1s and Si_3N_4 peaks have been fitted (see insert), and the stoichiometry is found by using the respective sensitivity factors for the compounds.

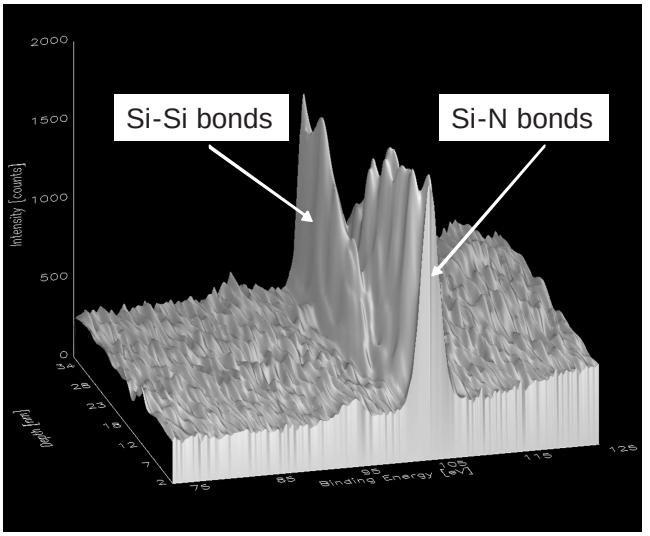

Figure 3.11: Si2p and Si_3N_4 concentrations (in arbitrary units) as a function of depth in a 34 nm thick sample (SRN on Si substrate) annealed at 1150 °C. The DCS/NH_3 ratio was 3.24, the N/Si ratio 1.1.

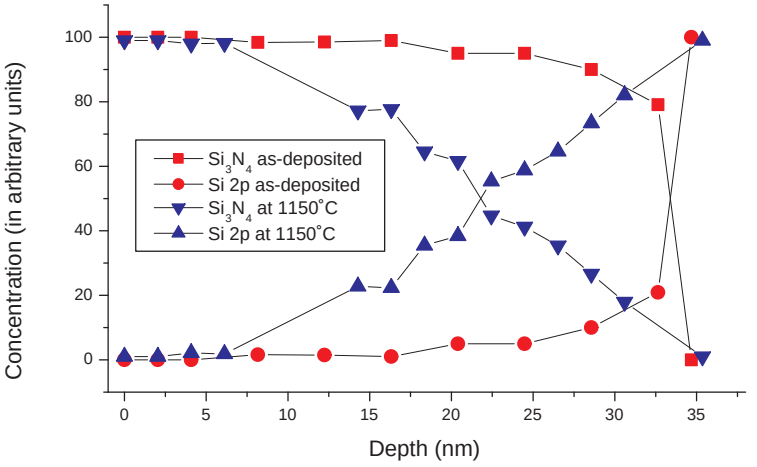

Figure 3.12: XPS depth profile of the concentrations of Si_3N_4 and Si2p in films on Si substrate as-deposited and annealed at 1150 °C.

3.2.3 X-ray photoelectron spectroscopy results: SRN on SiO_2 substrate

The following section describes XPS measurements performed in the same manner as in section 3.2.2. The only difference is that there is a 10 μm thermal oxide layer (SiO_2) between the SRN film and the Si substrate. In this section, the 'substrate' referred to is the complete sandwich of silicon wafer and SiO_2 layer.

The measurements show that the stoichiometry is not the same for SRN on thermal oxide and SRN on Si substrates (deposited in the same deposition batch). There is negligible Si diffusion, as expected because SiO_2 has been proven to be a good diffusion barrier for many materials [16]. No free Si gradient is seen near the interface between substrate and thin film.

However, a new effect is observed in the depth profiles: Diffusion of oxygen from the SiO_2 layer and into the SRN thin film. In figure 3.13 the depth profile of the concentration of Si_3N_4 and Si bound to O is shown. The amount of silicon bound to oxygen is non-existing at the surface but increases as the depth approaches the interface between SRN and substrate. Figure 3.14 shows depth profiles of the O1s and SiO_2 concentration. The SiO_2 signal clearly extends far into the thin SRN film, while the O1s signal drops as one probes deeper and deeper into the film. This means that, while the silicon diffusion has been eliminated, we now have oxygen diffusing from the substrate into the SRN film.

3.2.4 Spectral ellipsometry results

In order to make further investigations of the depth profile of the chemical composition observed above in section 3.2.2 another technique was used. Spectral ellipsometry measurements were performed on samples with a thickness of 0.6 μm.

The concentration gradient of free silicon described above in section 3.2.2 was confirmed by spectral ellipsometry. The data from the spectral ellipsometer measurements showed that the best-fitting model for the spectra was one which first has a pure silicon substrate, and then a layer of Si_3N_4 with a gradient of silicon ranging from 100% at the substrate interface to a few percent on the top (see figure 3.15). On top of this was a thicker layer with Si_3N_4 and a few percent Si. The intermedi-

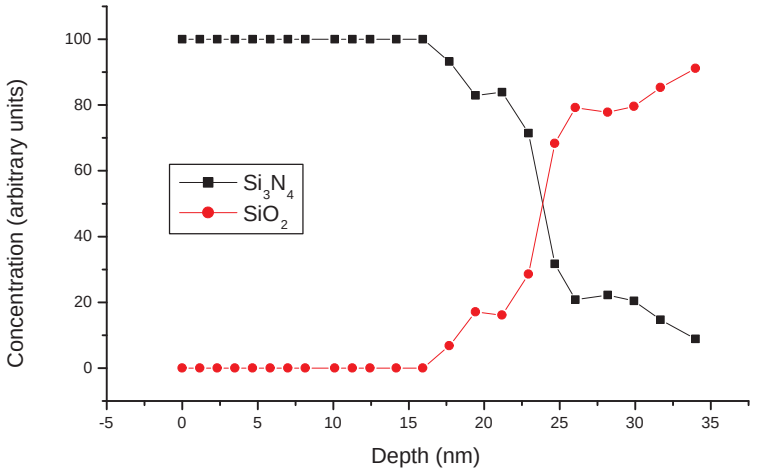

Figure 3.13: XPS depth profile of the concentration of Si_3N_4 and SiO_2 in 34 nm films on SiO_2 substrates annealed at 1150 °C.

ate layer (with the Si concentration gradient) fitted here was somewhat thicker than what was measured by XPS, but the total film thickness in the XPS experiment was only 34 nm, while the samples for spectral ellipsometry were 0.6 μm. The intermediate layer was found to be around 45 nm thick, the top layer with Si_3N_4 about 0.6 μm (in agreement with what was measured with the standard ellipsometer).

3.3 Discussion

Diffusion of silicon from the substrate into the SRN thin film is be a major problem for many applications. Therefore it is important to investigate the diffusion properties of silicon for different diffusion barriers between substrate and thin film.

When silicon rich nitride is used as a core layer for optical components, it is deposited on top of a thick layer of thermal oxide ($\sim$ 8-10 μm). It is then annealed at temperatures above 1100 °C to break any N-H bonds, which have absorption peaks in the wavelength band important for optical telecommunication (see section 4.2.2). Silicon clustering appears in

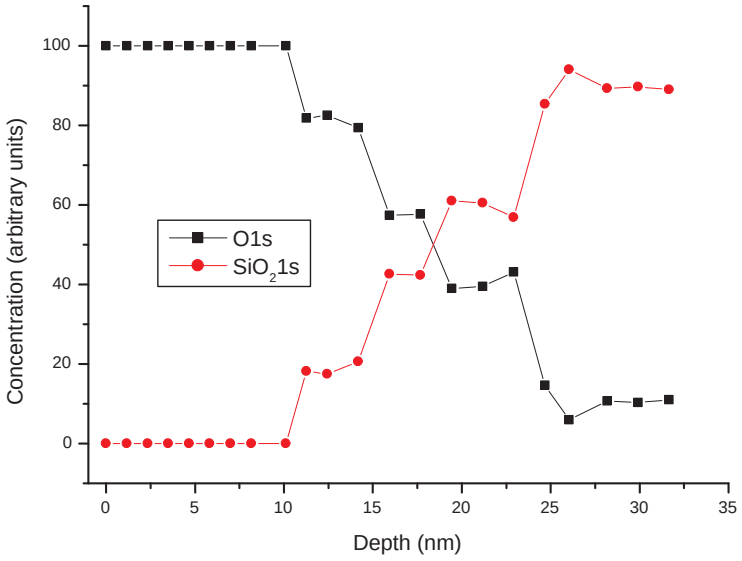

Figure 3.14: XPS depth profile of the concentrations of O1s and SiO_2 in 34 nm films on SiO_2 substrates annealed at 1150 °C.

Figure 3.15: A layer sketch of the structure of silicon nitride films on Si substrates after annealing at temperatures above 1110 °C.

the thin films when annealing is done above 1150 °C. This clustering is undesirable in waveguide materials because it can cause significant propagation loss. Previous experiments have shown lower losses for thin films annealed at 1100 °C [17], but higher losses at 1150 °C have been observed, and the silicon clustering effect is the most probable explanation. Consequently the annealing temperature should be chosen to be around 1100 °C to break the N-H bonds while minimizing silicon clustering.

The clustering can be prevented by a layer of silicon dioxide, which is a very good silicon diffusion barrier [16]; however, we find that it introduces a new problem, oxygen diffusion. The mechanisms triggering the out-diffusion of silicon and oxygen from the substrate into the thin film are not yet completely understood. One reason for the diffusion could be a large interface stress between the thin film and the substrate during the annealing process hereby activating the mobilization of silicon. This mechanism can be studied for example by $\sin^2\Psi$ X-ray diffraction [18]. Another contributor could be diffusion induced by the concentration gradient of silicon/oxygen from the substrate to the surface of the thin film. Another possibility is having excess silicon in the beginning of the deposition process. After some time the thin film relaxes, and more nitrogen can then be incorporated.

3.4 Conclusions

The chemical composition profile of silicon rich nitride thin films on Si and SiO_2 substrates has been determined by various tests using synchrotron radiation, XPS, RBS, and spectral ellipsometry. The results show that the silicon content in the thin films increases with increasing DCS/NH_3 ratio. Furthermore the silicon concentration increases in the films on Si substrates with increasing annealing temperature. Silicon diffusion was observed throughout the thin films on Si substrates when annealing was performed at temperatures above 1100 °C. Also, an intermediate layer was found between the thin film and the substrate with a linear concentration gradient of silicon. The thickness of this layer increases with annealing temperature, and therefore the total amount of silicon in the film increases at the same time.

The diffusion of silicon into the thin film can be prevented by depositing a layer of SiO_2 on top of the substrate, but at the expense of

introducing diffusion of oxygen from the substrate into the film. In optical components a SiO_2 layer between the Si substrate and the SRN film is used. Even though silicon diffusion from the substrate is eliminated by the oxide layer, there is still some diffusion of the free silicon in the films. The free silicon is expected (from synchrotron radiation experiments) to cluster into nano-clusters when annealing at high temperatures (above 1100 °C). Nano-clusters are expected to lead to optical losses (see section 4.1.1). The diffusion of oxygen from the thermal oxide into the SRN films might also contribute to the optical losses due to local variations in the refractive index (see section 4.1.1) or absorption due to O-H bonds (see section 4.1.2).

Chapter 3 references

[1] K. N. Andersen, P. C. Nielsen, and W. Svendsen. "Silicon rich nitride thin films and waveguides", in *Integrated Photonic Research/Optical Society of America,* IThA4, pp. 1–3, 2002.

[2] H. Toraya. "Quantitative phase analysis of alpha - and beta -silicon nitrides. i. estimation of errors", *Journal of Applied Crystallography*, vol. 32, no. 4, pp. 704–15, 1999.

[3] V. A. Gritsenko, K. S. Zhuravlev, A. D. Milov, H. Wong, R. W. M. Kwok, and J. B. Xu. "Silicon dots/clusters in silicon nitride: photoluminescence and electron spin resonance", *Thin Solid Films*, vol. 353, no. 1-2, pp. 20–24, 1999.

[4] V. A. Gritsenko, R. W. M. Kwok, H. Wong, and J. B. Xu. "Short-range order in non-stoichiometric amorphous silicon oxynitride and silicon-rich nitride", *Journal of Non-Crystalline Solids*, vol. 297, no. 1, pp. 96–101, 2002.

[5] V. A. Volodin, M. D. Efremov, V. A. Gritsenko, and S. A. Kochubei. "Raman study of silicon nanocrystals formed in SiN_x films by excimer laser or thermal annealing", *Applied Physics Letters*, vol. 73, no. 9, pp. 1212–14, 1998.

[6] H. Toraya. "Crystal structure refinement of α-Si_3N_4 using synchrotron radiation powder diffraction data: unbiased refinement strategy", *Journal of Applied Crystallography*, vol. 33, no. 1, pp. 95–102, 2000.

[7] M. Ohring. *The Materials Science of Thin Films.* Academic Press, Inc., 1992. ISBN 0-12-524990-X.

[8] L. R. Doolittle. "A semi-automiatic algorithm for rbs analysis", *Nucl. Instr. and Methods*, vol. B15, pp. 227–231.

[9] D. A. Shirley. "High-resolution X-Ray photoemission spectrum of the valence bands of gold", *Physical Review B*, vol. 5, no. 12, pp. 4709–4714, June 1972.

[10] A. R. Chourasia and D. R. Chopra. "A study of Si_3N_4 by XPS", *Surface Science Spectra*, vol. 2, no. 2, pp. 117–22, 1993.

[11] W. A. M. Harland and G. Tompkins. *Spectroscopic Ellipsometry and Reflectometry - A user's guide.* John Wiley and Sons, Inc., April 1999. ISBN 0-471-18172-2.

[12] M. Sekimoto, H. Yoshihara, and T. Ohkubo. "Silicon nitride single-layer X-ray mask", *Journal of Vacuum Science and Technology*, vol. 21, no. 4, pp. 1017–21, 1982.

[13] A. J. Flewitt, A. P. Dyson, J. Robertson, and W. I. Milne. "Low temperature growth of silicon nitride by electron cyclotron resonance plasma enhanced chemical vapour deposition", *Thin Solid Films*, vol. 383, no. 1-2, pp. 172–177, 2001.

[14] B. F. Hanyaloglu and E. S. Aydil. "Low temperature plasma deposition of silicon nitride from silane and nitrogen plasmas", *Journal of Vacuum Science & Technology A (Vacuum, Surfaces, and Films)*, vol. 16, no. 5, pp. 2794–803, 1998.

[15] R. E. Rocheleau and Z. Zhang. "Densification of plasma deposited silicon nitride films by hydrogen dilution", *Thin Solid Films*, vol. 220, no. 1, pp. 73–79, 1992.

[16] S. A. Guldberg-Kjær. *Planar waveguide amplifiers and laser in erbium doped silica.* Ph.D. thesis, COM, DTU, Denmark, December 1999. ISBN 87-900974-10-7.

[17] H. Mertens, K. N. Andersen, and W. Svendsen. "Optical loss analysis of silicon rich nitride waveguides", in *ECOC'02,* Copenhagen, Denmark, Paper P1.38, 2002.

[18] J. A. Ruud, A. Witvrouw, and F. Spaepen. "Interface stress in artificial multilayers", *Defects in Materials Symposium*, pp. 737–40, 1991.

Chapter 4

Optical Characterization of Thin Films

In the previous chapter some of the material characteristics of SRN films were presented. For integrated optical components it is important to have thin films with low, uniform stress and low optical loss. In order to produce optimal low-loss optical components, the thin films must be characterized optically before patterning and optimizing them for waveguide components. Due to fabrication effects (sidewall and surface roughness), the propagation loss in the final channel waveguide is expected to be higher than in a slab waveguide, i.e. in the thin film itself.

The thin films in this project were initially developed for making optical components for the telecommunication regime. This means that the losses have to be as low as possible in the C-band (wavelengths from 1530 to 1560 nm). Later on there has been an interest for using the film for other purposes, such as biological analysis, where the wavelength of interest is of the order of 400 - 700 nm.

There are two basic types of optical losses in waveguide components: intrinsic and extrinsic losses. Intrinsic losses include absorption (from vibrational, electronic, and molecular transitions) and Rayleigh scattering,. Extrinsic losses include absorption (due to impurities), scattering (volume, sidewall and interface roughness), and radiation (due to waveguide curvature, multimode effects). Losses due to waveguide fabrication effects (e. g. surface and sidewall roughness) and radiation will be described in section 5.2.

In thin films there are two major loss mechanisms: scattering and absorption losses. Scattering losses are due to surface scattering and imbedded scattering centers (clusters or particles), and absorption losses are due to internal excitations of vibrational oscillation modes of molecules, electronic resonances and phonons.

The optical absorption at wavelengths from 1500 to 1600 nm has been investigated, both in SRN thin films (section 4.2.2) and in SRN straight waveguides (section 5.4.1). One of the major concerns is absorption due to N-H vibration bonds (at 1510 nm), which have absorption peaks in the wavelength region of interest. It has been shown that annealing the SRN material can reduce the losses due to N-H absorption [1], but experiments have shown that annealing at very high temperatures ($> 1100\,^{\circ}$C) causes clustering in the material, as described in chapter 3. This clustering in adds to the loss of light due to intrinsic scattering. The clusters can be avoided by annealing at temperatures below $1110\,^{\circ}$C, i. e. the optimum temperature for reducing the amount of clusters while still breaking the N-H bonds must be controlled within this limitation. Since the losses should be kept as low as possible, it is important to understand the different loss mechanisms, such as the N-H vibration bonds, absorption, scattering due to scattering centers, Rayleigh scattering, and other possible sources of loss in order to reduce each of these contributions.

In the following sections, loss mechanisms in thin films (Rayleigh scattering, volume scattering, surface roughness, and absorption) will be described, as well as the techniques for measuring these losses (Fourier transform infrared spectroscopy (FTIR) and dual prism coupling).

4.1 Loss mechanisms in thin films

The intensity I of a propagating beam of light along the direction of propagation z is (see appendix C):

$$I(z) = I_0 e^{-\alpha(\lambda)z} \tag{4.1}$$

where α is the combined attenuation or loss parameter:

$$\alpha = \alpha_R + \alpha_{IM} + \alpha_{NH} + \alpha_{IR} + \alpha_{UV} + \alpha_{im} + \ldots \tag{4.2}$$

and

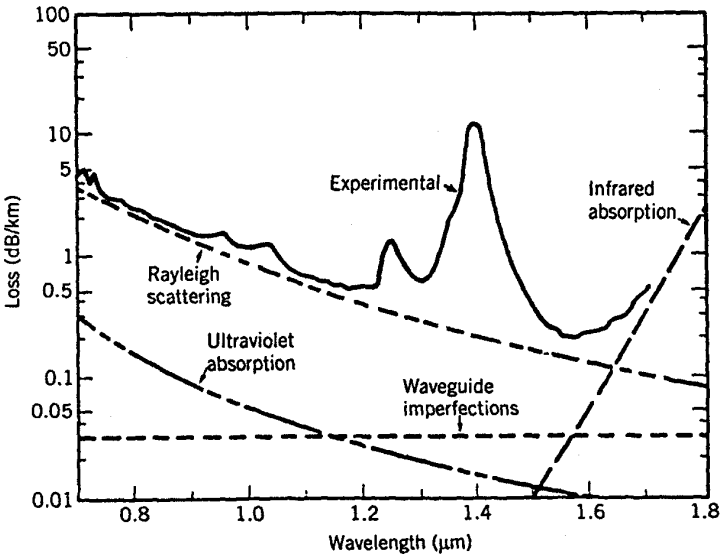

Figure 4.1: Loss spectrum of a single mode fiber [2]. The wavelength dependence of several fundamental loss mechanisms is also shown.

α_R is the Rayleigh scattering loss,
α_{IR} is the infrared absorption loss,
α_{UV} is the UV absorption loss,
α_{IM} is the loss due to imperfection,
α_{NH} is the N-H absorption loss,
and α_{im} is loss due to other impurities.

The wavelength dependence for several of these fundamental loss mechanisms for a single mode silica fiber is shown in figure 4.1.

4.1.1 Scattering losses

The following section is based on chapter 6 in "Integrated optics: theory and technology" by R. G. Hunsperger [3].

The three major types of scattering loss are: interface, volume, and Rayleigh scattering. Interface scattering (between core and cladding) can

be relatively high even for smooth surfaces, in particular for higher-order modes due to the strong interaction of the propagating waves with the slab waveguide surface. The loss coefficient for interface scattering depends on several parameters:

$$\alpha \propto \left(\frac{\sigma}{\lambda}\right)^2 \tag{4.3}$$

where σ is the variance of the roughness, and λ is the wavelength. This means that the losses can be reduced by reducing the roughness, or by increasing the wavelength.

As mentioned in section 2.2.1, the surface roughness for SRN films has been measured to be only around 3 nm. This is much smaller than the wavelengths used in the region of telecommunication ($\sigma/\lambda \ll 1$), i. e. losses from interface scattering can be assumed to be negligible at these wavelengths.

Volume scattering is caused by imperfections, such as voids, contaminant atoms and crystalline defects within the volume of the waveguiding material. The loss per unit length is proportional to the number of imperfections per unit length and is strongly dependent on the size of the imperfections relative to the wavelength of the light. Volume imperfections are usually so small compared to the wavelength and so few in number that the scattering loss is negligible compared to the interface scattering loss, but if clustering occurs as described above, volume scattering may have a major effect.

There are not very many particles in the material larger than the size detectable by optical microscopy (less than 4 per cm^2), so unless there are many nano-size particles, volume scattering losses can also be assumed to be negligible.

Rayleigh scattering is an elastic scattering which is due to local fluctuations in the refractive index. The scattering stems from inhomogeneities of a random nature occurring on a small scale compared to the wavelength of the light. The loss parameter due to Rayleigh scattering is:

$$\alpha_R = D \cdot \frac{1}{\lambda^4} \tag{4.4}$$

where D is a material dependent parameter. This means that the scattering loss decreases as the wavelength increases.

4.1.2 Absorption loss

Absorption loss can occur through two mechanisms: intraband electronic absorption and vibration absorption. The loss due to absorption is relatively small in amorphous thin films, unless contaminant atoms are present [3]. In SRN the incorporation of hydrogen from the process gasses during deposition (see section 2.2.1) gives absorption peaks around 1510 nm due to N-H vibrations [1].

The absorption can be calculated in several different ways, see for example [4] or [5].

The dispersion and absorption in isotropic dielectric materials are related through the Kramers-Kronig relations [4]:

$$\chi'(\nu) = \frac{2}{\pi}\int_0^\infty \frac{s\chi''(s)}{s^2-\nu^2}\mathrm{ds} \tag{4.5}$$

$$\chi''(\nu) = \frac{2}{\pi}\int_0^\infty \frac{\nu\chi'(s)}{\nu^2-s^2}\mathrm{ds} \tag{4.6}$$

where χ' and χ'' are the real (related to the refractive index) and imaginary part (related to the absorption) of the susceptibility χ and ν is the frequency. χ'' can be measured by X-ray Absorption Fine Structure (XAFS) and Diffraction Anomalous Fine Structure (DAFS). The χ'' spectrum is obtained experimentally from a sample via fluorescence measurements, and the corresponding χ' spectrum may be calculated by numerical integration using the above equation. This means that if either χ' or χ'' is known, then the other can be found through the Kramers-Kronig relations.

With k_0 denoting the wavenumber the refractive index n, absorption α and the susceptibility χ are related in the following way [4]:

$$n - i\frac{\alpha}{2\cdot k_0} = \sqrt{1+\chi'+i\chi''} \tag{4.7}$$

If n is known, then the absorption coefficient, α ($\alpha = \alpha_{IR} + \alpha_{UV} + \alpha_{im} + \ldots$), can be found by inserting χ' and χ''. The refractive index can be estimated using the Sellmeyer equations [4]:

$$n^2(\lambda) = 1 + \sum_j A_j \frac{\lambda_0^2}{\lambda_0^2+\lambda_j^2} \tag{4.8}$$

where the values A_j and λ_j can be found by fitting measured $n(\lambda)$, i. e. from dispersion data, to provide an estimate of the refractive index over a wide spectral range. The sum in equation (4.8) is over all resonance wavelengths. Using this estimate for the refractive index and inserting it into equation (4.7), the absorption coefficient can be found.

During deposition of SRN, precursors incorporate both hydrogen and nitrogen. This means that the thin films may contain significant amounts of N-H bonds. This is the case for both PECVD and LPCVD deposition [6]. N-H bonds have their intrinsic infrared absorption at 3020 nm. The first overtone is thus found at a wavelength of 1510 nm. The tail of this overtone leads to absorption losses in the wavelength region around 1550 nm. Annealing of the SRN layers at high temperatures can be used to largely remove the N-H bonds [6], [7], and [8].

Close to the resonant frequency the energy is absorbed from the incident wave, due to internal excitation. Energy is also absorbed from resonances and dissipated as heat. In SRN there is absorption due to N-H and Si-N bonds. In the following sections the importance of these absorption peaks will be investigated.

4.2 Loss measurements

The results in the following sections 4.2.1 and 4.2.2 were obtained by Hans Mertens.

4.2.1 Fourier transform infrared spectroscopy (FTIR)

Infrared spectroscopy is an analysis tool where the interaction of infrared radiation with the sample being investigated is characterized by monitoring the frequencies at which absorption of radiation occurs. By determining these frequencies it is possible to obtain information about the chemical composition of the sample, since the absorption of light at specific frequencies corresponds to the rotational and vibrational states of a specific compound [9].

In order for a particular rotational or vibrational mode to directly absorb infrared radiation, the motion associated with that mode must produce a change in the dipole moment of the compound. This requirement implies that bonds such as N-N and Si-Si bonds cannot be detected by

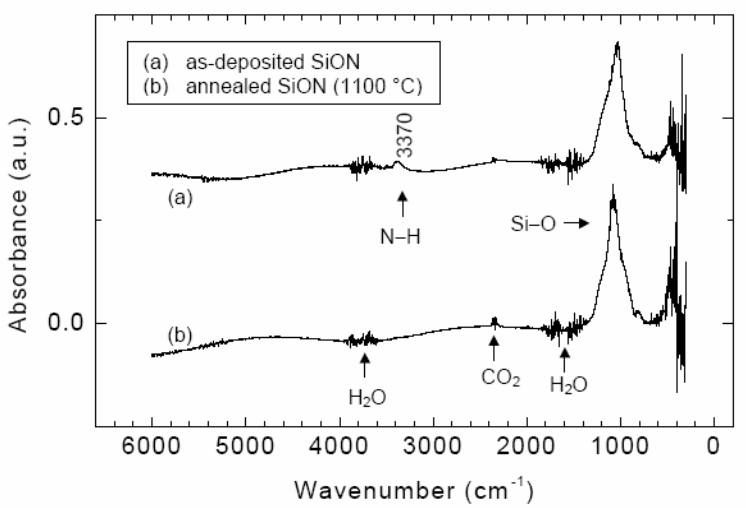

Figure 4.2: FTIR spectra of a 2 μm thick as-deposited and annealed SiON layers [10].

infrared spectroscopy, because they have no dipole moment. For solids, internal rotations are often limited, so the major type of interaction is vibrational. Fourier transform infrared (FTIR) spectroscopy is an implementation of infrared spectroscopy in which the spectrum is obtained on the basis of Fourier analysis. FTIR spectroscopy uses all the wavelengths at the same time, which means a signal-to-noise ratio enhancement (Fellgett's advantage, [9]). Another advantage of FTIR is the fact that the radiative throughput is larger than other infrared spectroscopic techniques. This beneficial effect is known as Jacquinot's advantage [9].

The FTIR spectrometer used for the experiment was an MIR 8000 from Oriel Instruments. The spectral range of this detector is 6000-300 cm^{-1} (1.7-28 μm), which means that fundamental N-H related absorption around 3300 cm^{-1} can be detected, but not the first overtone around 6600 cm^{-1}. The FTIR analysis provides absorption spectra as the one shown in figure 4.3. Peaks from Si-N, H_2O, and CO_2 can be seen in the scan.

The samples investigated by FTIR were as-deposited SRN and SiON layers containing N-H bonds. The main goal was to determine at which temperature annealing could reduce the losses due to these bonds. Unfortunately from a detection point of view, the analysis showed that the

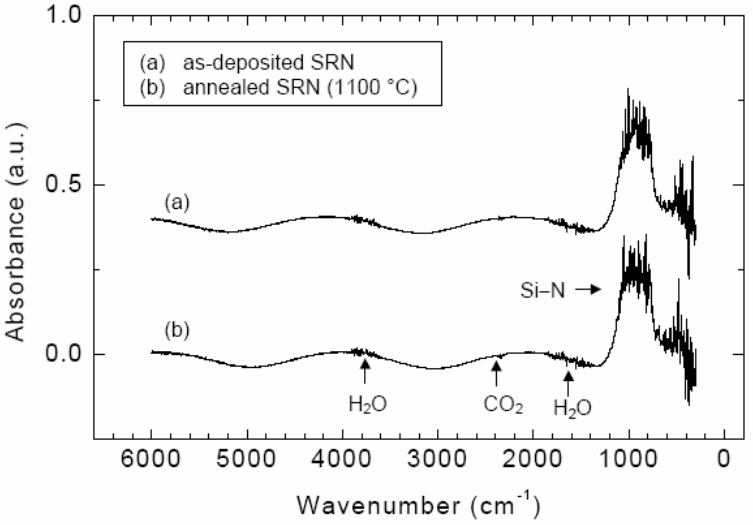

Figure 4.3: FTIR spectrum of a 1.2 μm thick as-deposited and annealed SRN layers [1].

amount of N-H bonds in our as-deposited SRN layers was lower than the detection limit of FTIR (see figure 4.3) - which is, of course, actually, as our aim is to produce low-loss materials. This observation was in agreement with published results [11]. Also the peak from Si-H bonds around 2336.6 cm^{-1} could not be seen. Therefore, another technique with higher resolution had to be used, for example be by dual prism coupling. The following section discusses results from such an analysis.

4.2.2 Dual prism coupling

Optical loss spectra of an SRN slab waveguide have been measured in the wavelength region of interest using dual prism coupling [1]. This characterization technique provides information about the propagation loss in slab waveguides as a function of wavelength. This information is useful as a characterization tool for the deposition and annealing process since losses due to waveguide fabrication are excluded. As mentioned above, it is important to identify the different loss mechanisms in order to clarify whether the losses can be reduced by altering the processing

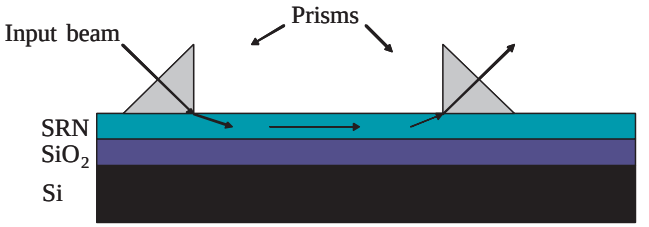

Figure 4.4: The principles of the dual prism setup.

(photolithography and RIE) of the waveguides or the material.

The principle of the dual prism technique is shown in figure 4.4. An incoming beam of light is coupled into the thin film through a prism. Rutile (TiO_2) prisms had to be used due to the high refractive index of SRN. Another prism for outcupling was placed in the direction of the propagating beam. The in- and outcoupling intensities were maximized by adjusting the pressure of the prism on the sample. The attenuation (as a function of wavelength) was measured as a function of the distance between the in- and outcoupled beams. In this way both the incoupling and propagation losses (dB/cm) can be determined.

The setup used was located at the University of Twente, The Netherlands. 1.2 μm-thick SRN layers deposited onto thermally oxidized (10 μm) silicon wafers were used for this analysis. A 2 μm thick as-deposited PECVD-grown (at 250 °C) SiON layer with a refractive index of 1.52 on similar wafers was used as a reference. FTIR analysis of the SiON films showed that they contained large amounts of N-H absorption. This was a good reference for comparing the losses in the same way as was done with FTIR. Figure 4.5 shows a wavelength spectrum of the propagation loss of both an as-deposited SRN layer and an as-deposited SiON layer.

In figure 4.5 it is seen that the propagation loss in as-deposited SRN is much smaller than in PECVD-grown SiON. From the FTIR results it is known that there is a lot of absorption due to N-H bonds in SiON films (see figure 4.2). Therefore it is expected that these bonds will also show losses when measuring with dual prism coupling. The larger loss of SiON in this region (1470-1570 nm) can be assumed to originate from N-H bonds since no other vibration modes are located in that wavelength span. It can be seen that the absorption peaks in SiON and SRN are not centered

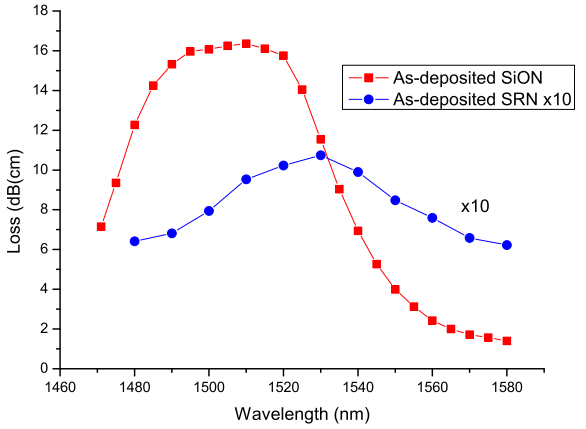

Figure 4.5: Propagation loss spectrum of an as-deposited SRN slab waveguide and an as-deposited SiON slab waveguide. Note that the values for SRN have been multiplied by 10 to make the comparison easier.

around the same wavelength. This is probably because of the difference in hydrogen bonding interactions due to the different structure and density of the films (one is PECVD grown at 250 °C, and the other LPCVD grown at 835 °C) [12]. It has been seen with other deposition techniques that the amount of hydrogen is highly dependent on the deposition temperature [12]. The higher the deposition temperature is the lower the hydrogen content is. This is in good agreement with the FTIR measurements.

A scan of the N-H related absorption peak in as-deposited and annealed SRN is shown in figure 4.6. It can be seen that there is a small absorption peak and that the height of the peak decreases at the annealing temperature of 1100 °C. The N-H peak does not disappear completely, but it might be reduced further by annealing at even higher temperatures [13], [8]. 1100 °C was chosen, however, such that clustering and hereby scattering was also minimal. The propagation loss at a wavelength of 1580 nm is only 0.60 ± 0.05 dB/cm.

An attempt was made to measure the propagation loss of SRN films in a much larger wavelength regime (300 - 1700 nm) and annealed at higher temperatures. Unfortunately, due to a leak in the vacuum of the LPCVD furnace, it was not possible to fabricate samples with a sufficiently low

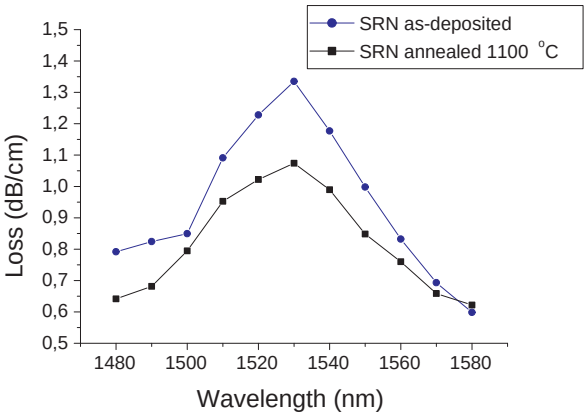

Figure 4.6: Propagation loss spectrum of an as-deposited SRN slab waveguide and an SRN slab waveguide that has been annealed at 1100 °C [1].

number of particles. The particles in the films were numerous and around 1 μm in size. Hence, when trying to couple light into and out of the thin films, too much light was scattered away to actually get enough intensity for analysis.

4.3 Conclusions

The sources of optical loss have been investigated, primarily by the dual prism technique in as-deposited and annealed SRN films. A minor absorption peak was observed around 1530 nm and was attributed to N-H absorption. The propagation loss could be reduced by annealing, but only to a certain degree. It might be possible to achieve this by annealing at even higher temperatures, but this may cause other problems because of clustering. It has been observed that clusters start to form at temperatures above 1100 °C, so this temperature seems to be the best compromise between reducing losses due to N-H absorption while avoiding clusters, which give problems with scattering.

Chapter 4 references

[1] H. Mertens, K. N. Andersen, and W. Svendsen. "Optical loss analysis of silicon rich nitride waveguides", in *ECOC'02,* Copenhagen, Denmark, Paper P1.38, 2002.

[2] T. Miya, Y. Terunuma, T. Hosaka, and T. Miyashita. "Ultimate low-loss single-mode fibre at 1.55 μm", *Electronics Letters*, vol. 15, no. 4, pp. 106–8, 1979.

[3] R. G. Hunsperger. *Integrated optics: theory and technology.* Advanced texts in physics. Springer, Berlin, Fifth edition, 2002. ISBN 3-540-43341-4.

[4] R. Syms and J. Cozens. *Optical guided waves and devices.* McGraw-Hill, London, 1992. ISBN 0077074254.

[5] B. E. A. Saleh and M. Teich. *Fundamentals of Photonics.* Wiley and Sons Inc., 1991. ISBN 0471839655.

[6] K. Wörhoff, P. V. Lambeck, and A. Driessen. "Design, tolerance analysis, and fabrication of silicon oxynitride based planar optical waveguides for communication devices", *Journal of Lightwave Technology*, vol. 17, no. 8, pp. 1401–1407, 1999.

[7] R. Germann, H. W. M. Salemink, R. Beyeler, G. L. Bona, F. Horst, I. Massarek, and B. J. Offrein. "Electrochemical/chemical deposition and etching - silicon oxynitride layers for optical waveguide applications", *Journal of the Electrochemical Society*, vol. 147, no. 6, pp. 2237–2241, 2000.

[8] C. H. Henry, R. F. Kazarinov, H. J. Lee, K. J. Orlowsky, and L. E. Katz. "Low loss Si_3N_4-SiO_2 optical wavegudies on Si", *Applied Optics*, vol. 26, no. 13, pp. 2621–2624, July 1987.

[9] P. R. Griffiths and J. A. De Haseth. *Fourier Transform Infrared Spectrometry.* John Wiley and Sons, New York, USA, April 1986. ISBN 0-471-09902-3.

[10] H. Mertens. *Silicon rich nitride (SRN) of optical waveguide applications.* Master thesis, Technische Universiteit Eindhoven, The Netherlands, August 2002.

[11] M.-C. Cheng, C.-P. Chang, W.-S. Huang, and R.-S. Huang. "Ultralow-stress silicon-rich nitride films for microstructure fabrication", *Sensors and Materials*, vol. 11, no. 6, pp. 349–58, 1999.

[12] L. S. Patil, R. K. Pandey, J. P. Bange, S. A. Gaikwad, and D. K. Gautam. "Effect of deposition temperature on the chemical properties of thermally deposited silicon nitride films", *Optical Materials*, vol. 27, no. 4, pp. 663–670, 2005.

[13] F. Ay and A. Aydinli. "Comparative investigation of hydrogen bonding in silicon based PECVD grown dielectrics for optical waveguides", *Optical Materials*, vol. 26, no. 1, pp. 33–46, 2004.

Chapter 5

Characterization of Waveguides

Before making waveguide structures in thin films it is essential to know the basic properties of the films. In chapters 3 and 4, SRN thin films have been investigated with respect to material and optical characteristics. When these characteristics are well known they can be taken into consideration when designing components based on these films. Chapter 2 describes the fabrication of waveguides in SRN thin films with low stress, well-defined line width reduction, vertical sidewalls, and low surface and sidewall roughness.

After completing all the processing steps described in chapter 2 the optical components are characterized. One major concern is the propagation loss in the straight channel waveguides. If this differs sufficiently from the propagation loss in the films (slab waveguides), further process development has to be carried out.

In the following chapter waveguides will be characterized with respect to propagation and bend losses.

5.1 Waveguides

The basic physical description of the behavior of light in waveguides can be found in textbooks on integrated optics, see for example [1] or [2]. The wave equation is found from Maxwell's equations, and the solutions

provide the propagation constant for any given mode, and detailed information on the mode profile (see appendix C).

5.2 Loss mechanisms in waveguides

The three main loss mechanisms in optical waveguides are: scattering losses (see section 4.1.1), absorption losses (see section 4.1.2), and radiation losses. The first two types refer mainly to the properties of the thin film layers (slab waveguides), while the latter refers to the loss of modes propagating in a waveguide.

Sidewall roughness of waveguides can be a major loss factor if the roughnesses are of the order of the wavelength of the propagating mode [1]. It is difficult to measure the actual roughness of a sidewall. However, this type of roughness has been investigated visually by SEM. As can be seen from the SEM image in figure 2.9 the sidewall looks smooth. The losses from sidewall roughness will be one of the contributions to the total propagation loss. This will be discussed in more detail in section 5.4.1.

Losses from planar or straight channel waveguides are generally negligible for well confined modes far from cut-off. At cutoff all the energy is transferred to substrate radiation modes (see appendix C). The radiation of higher-order modes is greater than lower-order modes since higher-order modes are always either beyond or are at least closer to cut-off [1]. Irregularities and inhomogenities in waveguides can cause mode conversion, so that the energy is coupled from lower to higher-order modes [3].

Figure 5.1 shows the approximate cut-off of the first anti-symmetric mode of square cross section SRN waveguides [4]. The calculations have been done by Hugh Philipp using the finite difference method (using BBV Olympios Software and the Wave Matching Method [5]). It can be seen in figure 5.1 that waveguide cross section dimensions of around 0.6 μm x 0.6 μm result in only the fundamental mode being guided (single mode), thus eliminating problems with coupling between modes and modal dispersion.

Radiation loss has to be taken into account when dealing with channel waveguide structures with bends. This is due to the distortions of the optical field that occur when guided waves travel through a bend. Most optical integrated circuits have components with bent waveguides, so bending loss is a very important factor.

The minimum allowed bending radius of a waveguide is usually lim-

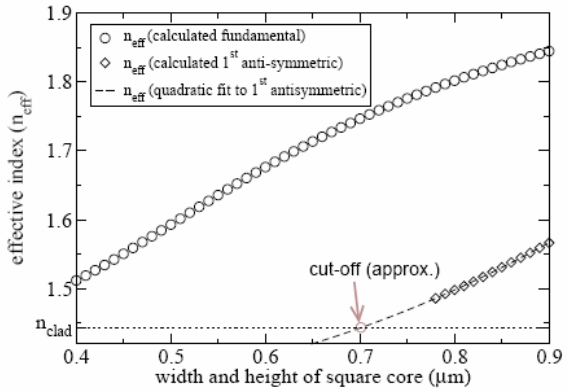

Figure 5.1: The approximate cut-off of the first anti-symmetric mode of square cross section SRN waveguides [4].

ited by radiation loss and not by fabrication tolerances [1]. Marcatili and Miller [6] show a comprehensive analysis method for the radiation loss: In order for the phase front to be preserved in a bent waveguide, the tangential phase velocity of the propagating modes has to be proportional to the distance from the center of the curvature. In figure 5.2 a curved waveguide, with refractive index n_2, radius of curvature R, and propagation constant β is shown. The phase velocity has to exceed the velocity of unguided light (in the surrounding cladding) in order to preserve the phase front. The critical radius beyond which this happens is R + X_r, where [1]:

$$X_r = \frac{\beta_z - \beta_0}{\beta_0} R \tag{5.1}$$

Here, β_0 is the propagation constant of unguided light in the cladding, and β_z is the propagation constant in waveguide at radius R. This means that in order for the mode to propagate in the waveguide, the radius of curvature has to be larger than R + X_r if the mode is to be guided through the bend.

The radiation loss coefficient, α_R (see section 4.1), depends exponentially on the radius of curvature, waveguide dimensions, and shape of the optical mode [1]:

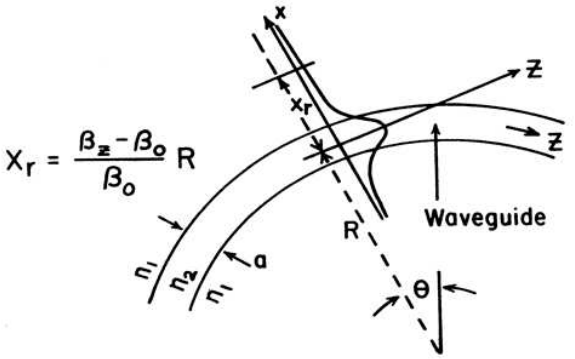

Figure 5.2: An illustration of the Marcatili and Miller [6] velocity approach for finding the radiation loss. The core material has refractive index n_2, and the surrounding cladding has n_1. R is the waveguide radius, β_0 = propagation constant of unguided light in the cladding, and β_z = propagation constant in waveguide at radius R [1].

$$\alpha_R = C_1 \exp(-C_2 R) \tag{5.2}$$

where C_1 and C_2 are constants which depend on the dimensions of the waveguide, and on the shape of the optical mode. It is possible to calculate the minimum radius (for fixed wavelength and waveguide geometry and index step) for a certain allowed bend loss. The minimum allowed bending radius is strongly dependent on the difference in refractive index between the core and the cladding material. Since the propagation loss of straight SRN waveguides (with SiO_2 cladding) is typically 0.6 ± 0.3 dB/cm (see section 5.4.1) a loss less than 0.1 dB due to bends can be tolerated. For SRN waveguides the minimum bend radius has been calculated to be around 25 μm for the bend loss to be less than 0.1 dB [4].

5.3 Measurement setup

Coupling of light into optical components can be done in several different ways. The technique chosen here to couple the light in and out of the waveguide components is butt-coupling with fibers.

The equipment used was a tunable laser (TLS) synchronized with an optical spectrum analyzer (OSA) (see figure 5.3). High precision piezo-

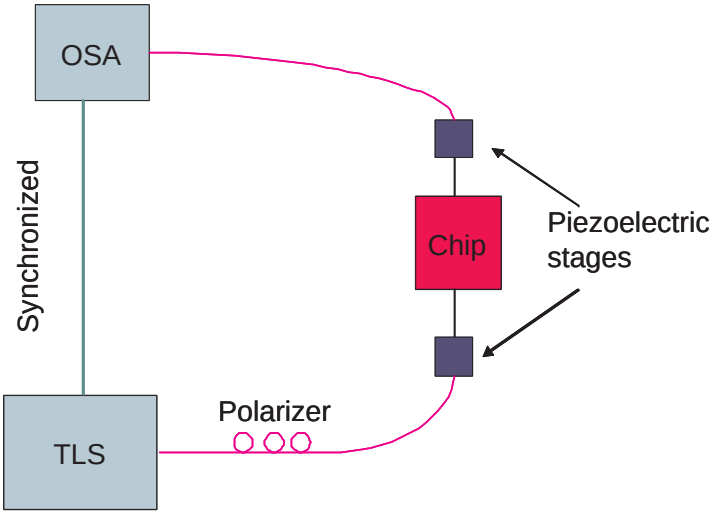

Figure 5.3: The optical characterization setup.

electrically controlled stages were used to align the fiber cores to the waveguide cores, i. e. to optimize the intensity level of the in- and out-coupled light. The polarization of the light was switched between TE and TM using a polarization controller.

Due to the high index step between the SRN waveguides and the surrounding cladding, it was necessary to use fibers with high numerical aperture (NA) and small spot size to couple light in and out of the waveguides. The high NA fibers, which had a spot size of 3 μm, was spliced on to the standard fibers connected to the OSA and the TLS.

5.3.1 Cutback

The idea behind cutback measurements is that the losses due to coupling (between fiber and waveguide) and propagation (in the waveguide) can be separated from each other. In the procedure, the attenuation in straight waveguides is measured first. Then a piece of the waveguide is cut off by dicing or cleaving and the attenuation in the remainder is measured. This is done for several different waveguide lengths. By plotting the attenuation as a function of waveguide length, the propagation loss can be found as the slope, and the coupling loss is the loss extrapolated to

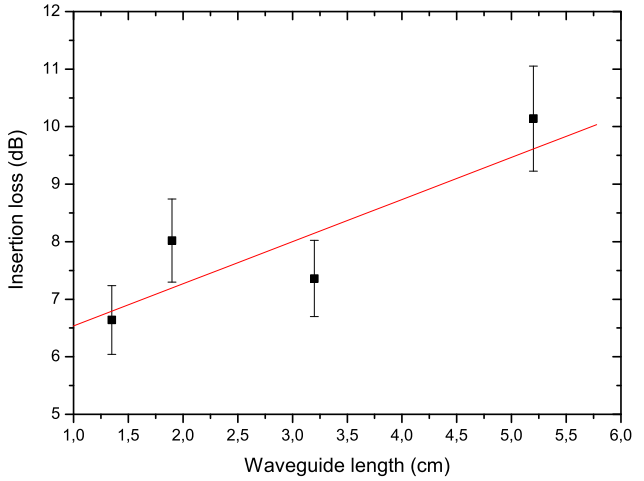

Figure 5.4: Cutback measurements performed at 1542.9 nm of a waveguide annealed at 1100 °C [7].

zero waveguide length. An example of this is shown in figure 5.4.

It is assumed that the coupling between the fiber and the waveguide remains constant during the measurements. This is quite difficult to achieve in reality, because the coupling is sensitive to the alignment between fiber and waveguide and to small irregularities in the end facets of the waveguides.

5.4 Results

5.4.1 Buried channel waveguides

Optical loss measurements were carried out on SRN waveguides with a refractive index of 2.06 measured at 1550 nm. The index step Δn between the core and the cladding was 0.602 at 1550 nm. The height of the waveguide cross sections was 0.6 μm and in some cases 1.3 μm, and the width varied between 0.6 and 2 μm. This means that some of the measured waveguides were multimode. However, since the loss

measurements were carried out on straight waveguides this did not affect the measurement to a first order approximation.

The cutback method (described in section 5.3.1) was used to determine the propagation loss in SRN channel waveguides. These waveguides were fabricated from the same type of films used for the dual prism coupling measurements discussed in section 4.2.2. The cutback was performed by dicing the waveguides. The height of the SRN waveguide was 1.3 μm and the width 8 μm. In figure 5.4 a plot of the insertion loss (dB) as a function of the waveguide length is shown. By fitting the data, the propagation loss was calculated to be 0.73 $\pm$ 0.27 dB/cm, and the coupling loss was 5.80 $\pm$ 0.76 dB. The errors in the measurement were found by repeated measurements. The propagation losses of the slab (described in section 4.2.2) and channel waveguides are the same within the uncertainty of the experiments. Hence, the waveguide loss may be attributed to absorption loss solely, and the contribution to the scattering loss from sidewall roughness can be neglected. This means that the fabrication of channel waveguides has reached an optimum where on extra losses are induced.

Since the above measurements have been performed the cleanroom processing has be optimized further, and the amount of particles has been reduced. Cleaving rather than dicing of the waveguides has been used for the cutback measurements. These new and yet unpublished results are shown in figure 5.5. The height of the SRN waveguide was 0.6 μm and the width 0.7 μm (1 μm on the mask). The figure shows a plot of the calculated propagation loss (dB/cm) as a function of the wavelength for annealed and unannealed waveguides. An example of how the propagation loss was calculated is shown in figure 5.6. At the wavelength of 1550 nm the propagation loss (the slope of the linear fit) is 0.44 $\pm$ 0.24 dB/cm for an annealed waveguide. Each point on the graph in figure 5.5 is the calculated in this way for wavelengths from 1520 to 1620 nm. It can be sen on the graph that the propagation loss is constant within the uncertainty in this wavelength region. For comparison, Daldosso et al. [8] have recently published results from similar waveguides also measured by the cutback technique. They observe propagation losses of 4.5 to 6 dB/cm at 1544 nm.

The propagation loss at 1550 nm of the annealed waveguide was calculated to be 0.44 $\pm$ 0.24 dB/cm and 1.50 $\pm$ 0.11 dB/cm for the unannealed

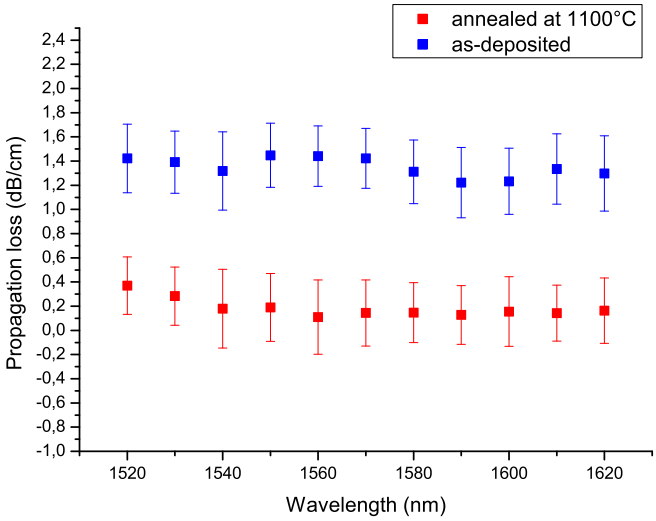

Figure 5.5: Propagation loss of annealed and unannealed SRN waveguides as a function wavelength measured by the cutback method.

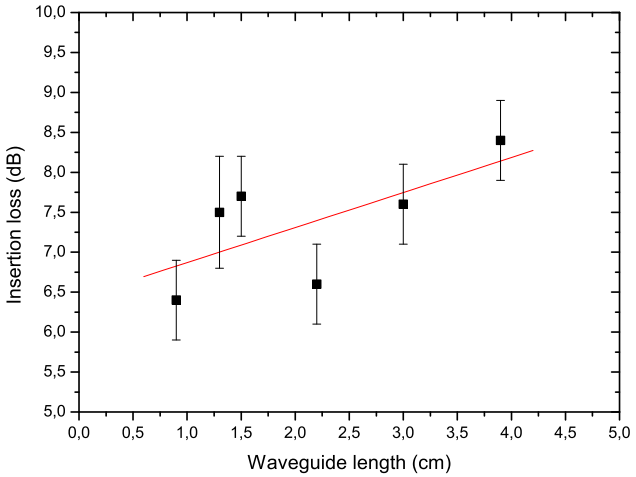

Figure 5.6: Cutback measurements performed at 1550 nm of a waveguide annealed at 1100 °C fabricated with a new process.

waveguide. The uncertainty of the values in figure 5.5 and 5.6 were found by repeated measurements. From figure 5.5 it is observed that the propagation loss can be reduced by 1 dB/cm by annealing at 1100 °C. This is in good agreement with the observations in the slab waveguides in section 4.2.2. The coupling losses were typically around 4 dB, which is 2 dB less than the above described samples. The reduction of the coupling loss is attributed to the better end facets achieved by cleaving rather than dicing.

In order to further investigate the influence of the material properties observed at elevated temperatures in chapter 3 waveguides were annealed at 1150 °C. This annealing of the waveguides gives even higher losses than what is observed for unannealed samples. The loss is attributed scattering from clusters and a possible roughening of the waveguide sidewalls from clusters during etching (as described in chapter 3).

5.4.2 Waveguides with bends

Controlling the curvature loss of optical components is critical. In order to determine the critical radius of curvature (equation (5.1)) for a bend loss of a maximum of 0.1 dB, several waveguides with different radii of curvature and with a varying number of bends from two to ten were measured for TE polarized light. There was no measurable difference in insertion loss as a function of the number of bends in a waveguide even for the smallest radius of 20 μm. From these measurements it was concluded that the bend loss for one 90 ° bend with 20 μm radius is below 0.1 dB [9]. These results are in agreement with the predictions mentioned in section 5.2. The critical radius of curvature from theoretical predictions and measurements match. This means that the propagation loss in the waveguides is the dominating loss mechanism (as long as the radius of curvature is kept above 20 μm).

The difference in losses for TE and TM polarized light has been investigated by Hugh Philipp [4]. He has shown that the TM mode is more lossy than the TE mode for waveguide geometries varying between a width of 0.7 to 0.9 μm and a height of 0.33 and 0.61 μm. He has also shown that the magnitude of the loss is associated with the waveguide geometry. The larger the cross section was of the waveguide the smaller the loss tended to be.

5.5 Conclusions

Slab and channel waveguides processed under the same conditions have a propagation loss in the same range (0.7 ± 0.3 dB/cm). Since the difference in the losses is within the measurement uncertainty, it means that the processing of waveguide components is optimized to a degree where no extra losses are induced.

Further process improvement and a reduction of the number of particles has reduced the propagation loss at 1550 nm even further, from 0.73 $\pm$ 0.27 dB/cm to 0.44 $\pm$ 0.24 dB/cm. This is a major achievement and is (to the knowledge of the author) the lowest loss observed for single mode buried SRN channel waveguides. Furthermore, it has been observed that the propagation loss can be lowered by 1 dB/cm by annealing at 1100 °C. This is seen for both slab and channel waveguides. The reason for this

reduction in loss has been attributed the breaking of N-H bonds.

Annealing at even higher temperatures, 1150 °C, the propagation loss increases in channel waveguides. There is a trade off between annealing at higher temperatures hereby breaking more N-H bonds, while at the same time not forming clusters which lead to scattering losses. The losses from scattering exceed the benefits from breaking N-H bonds when annealing at 1150 °C, and therefore the total propagations is higher than before annealing.

Experimentally, waveguide bends as small as 20 μm in curvature has proven not to induce excess loss. This bending radius is in good agreement with theoretical predictions. The bend loss is smaller than 0.1 dB per 90 degree bend for radii of curvature down to 20 μm.

This chapter has described some very basic properties of straight and curved channel waveguides. Knowing these characteristics is crucial when making more complicated structures such as ring resonators, which will be described in the following chapter.

Chapter 5 references

[1] R. G. Hunsperger. *Integrated optics: theory and technology.* Advanced texts in physics. Springer, Berlin, Fifth edition, 2002. ISBN 3-540-43341-4.

[2] R. Syms and J. Cozens. *Optical guided waves and devices.* McGraw-Hill, London, 1992. ISBN 0077074254.

[3] D. Marcuse. "Mode conversion caused by surface imperfections of a dielectric slab waveguide", *Bell System Technical Journal*, vol. 48, no. 10, pp. 3187–215, 1969.

[4] H. T. Philipp. *High-Index Contrast Silicon Rich Silicon Nitride Waveguides and Devices.* Ph.D. thesis, Research Center COM, Technical University of Denmark, Oersteds Plads, Build. 345V, DK-2800 Kgs. Lyngby, Denmark, October 2004. ISBN 87-90974-55-7.

[5] M. Lohmeyer. "Vectorial wave-matching mode analysis of integrated optical waveguides", *Optical and Quantum Electronics*, vol. 30, no. 5, pp. 385–396, 1998.

[6] E. A. J. Marcatili and S. E. Miller. "Improved relations describing directional control in electromagnetic wave guidance", *Bell System Technical Journal*, vol. 48, no. 7, pp. 2161–88, 1969.

[7] K. N. Andersen, P. C. Nielsen, and W. Svendsen. "Silicon rich nitride thin films and waveguides", in *Integrated Photonic Research/Optical Society of America,* IThA4, pp. 1–3, 2002.

[8] N. Daldosso, M. Melchiorri, F. Riboli, F. Sbrana, L. Pavesi, G. Pucker, C. Kompocholis, M. Crivellari, P. Bellutti, and A. Lui. "Fabrication and optical characterization of thin two-dimensional Si3N4 waveguides", *Materials Science in Semiconductor Processing*, vol. 7, no. 4-6, pp. 453–458, 2004.

[9] K. N. Andersen, W. E. Svendsen, R. K. Sandberg, H. T. Philipp, and J. Hübner. "Silicon rich nitride micro-resonators", *11th European Conference on Integrated Optics*, vol. 1, pp. 43–6, 2003.

Chapter 6

Ring resonators

Digital optical filters are a major field of interest in telecommunication, because of the fact that nearly arbitrary filter functions can be built from a few rather simple building blocks using digital signal processing theory [1]. One of the main disadvantages in realizing these filters has been the limitation in bending radii, limiting the free spectral range (FSR) of the resonators and at the same time leading to large and thereby expensive components. Using SRN as waveguide material, resonators having a factor of hundred smaller bend radii than normally obtained in silica based components can be realized. This means that the required area for one resonator loop is nearly four orders of magnitude smaller allowing in principle a 1000 times higher integration density of integrated optical components. At the same time the much smaller bending radii allow for the FSR for SRN components to be so large that it exceeds than of the channel spacing in wavelength division multiplexing systems. The typical bending radius for silica waveguides is in the order of cm, which results in a FSR of around 0.01 nm [2], [3]. On the other hand, increasing the refractive index to that of silicon, gives a FSR of around 20 nm [4], [5]. This is in the same order as SRN components, but the processing tolerances are much harder to meet.

Although the coupling and propagation losses are high compared to standard silica on silicon waveguide they do not pose a significant problem. Since the high index step between SRN and SiO_2 cladding makes it possible to make the components much smaller. The loss per component is in the same order of magnitude or smaller.

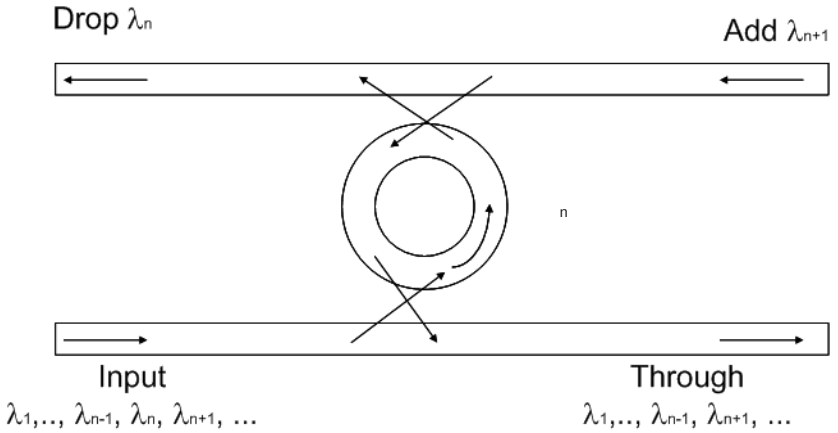

Figure 6.1: Add drop filter.

6.1 Ring resonator model

A ring resonator allows only specific wavelengths to couple into the resonator. The allowed wavelengths depend on the size of the ring resonator. The most simple component using ring resonators is the add-drop filter shown in figure 6.1, where a waveguide ring is sandwiched between two straight waveguides. The light is coupled into one of the straight waveguides which then couples to the ring. Depending on the optical length[1] of the ring only certain discrete wavelengths (a multiple of the vacuum wavelength) can interfere constructively in the ring. These wavelengths can then be coupled out in the other straight waveguide. The distance between two resonance dips is called the free spectral range (FSR) and can be approximated to:

$$FSR = \frac{\lambda^2}{n_g L} \tag{6.1}$$

where λ is the vacuum wavelength of the light, n_g is the effective group index at this wavelength, and L is the physical length of the ring.

The coupling between a straight waveguide and a ring a schematic is illustrated schematically in figure 6.2. In the following CW light is

[1]The optical length is defined at the effective index of the waveguide times the physical length of the ring.

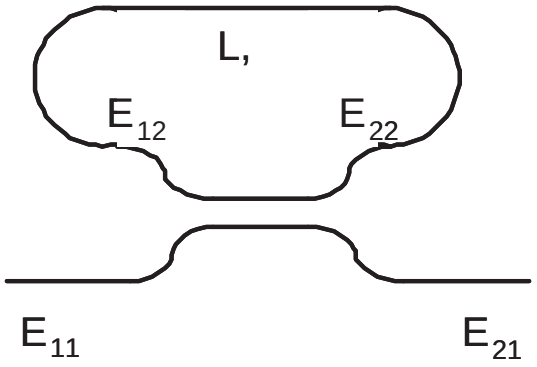

Figure 6.2: Coupling scheme used for the resonators [6].

assumed. A fraction (κ) of the intensity of the propagating field in the straight waveguide mode (E_{11}) is coupled evanescently with the mode field yielding a field (E_{22}) that propagates in the ring resonator. While this field propagates in the resonator the modal amplitude decreases due to the propagation and bend loss of one round trip in the resonator (fractional loss γ) yielding a field (E_{12}), which couples out of the resonator with a coupling coefficient (κ). This field interferes with the field in the straight waveguide yielding a field (E_{21}) now propagating in the straight waveguide.

As described in section 5.4.2 the curvature loss of the SRN waveguide bends is below 0.1 dB when the radius of curvature is kept above 25 μm. This means that the propagation loss in the waveguide is the dominating loss mechanism within the resonator.

Writing the electric field equations:

$$\begin{aligned} E_{21} &= E_{11}\sqrt{1-\kappa} - jE_{12}\sqrt{\kappa} \\ E_{22} &= E_{12}\sqrt{1-\kappa} - jE_{11}\sqrt{\kappa} \\ E_{12} &= E_{22}\sqrt{1-\gamma}\exp\left(j\cdot 2\pi\frac{L\cdot n_{eff}(\lambda)}{\lambda}\right) \end{aligned} \tag{6.2}$$

where L is the physical length of the resonator, and n_{eff} is the effective group index. By solving these equations the output intensity is found:

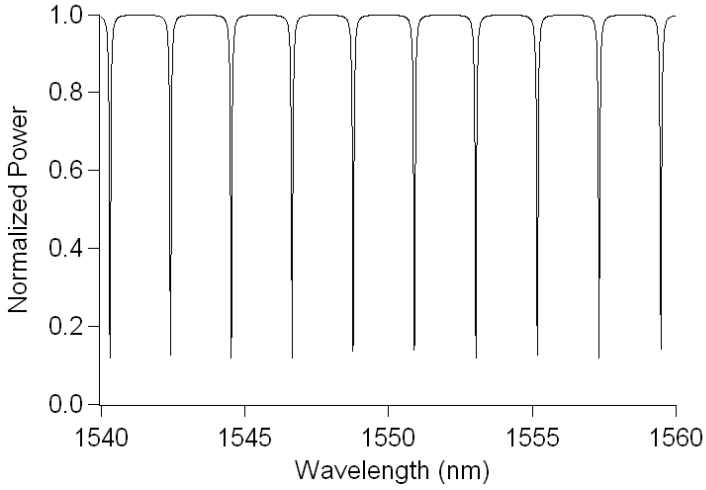

Figure 6.3: Normalized power versus wavelength, calculated from equation 6.3.

$$\begin{aligned} I_{out} &= E_{21} \cdot E_{21}^{*} \\ &= |E_{11}|^2 \frac{2-\kappa-\gamma-2\sqrt{1-\kappa}\sqrt{1-\gamma}\cos(2\pi\frac{L\cdot n_{eff}(\lambda)}{\lambda})}{2-\kappa-\gamma+\kappa\gamma-2\sqrt{1-\kappa}\sqrt{1-\gamma}\cos(2\pi\frac{L\cdot n_{eff}(\lambda)}{\lambda})} \end{aligned} \quad (6.3)$$

As can be seen from equation 6.3 plotted in figure 6.3, the deepest resonances (difference in maximum and minimum output intensity) occur when the fractional loss γ and the coupling coefficient κ are close to being equal. If the ring is completely lossless then all power transmitted at the resonance wavelength can be extracted. Note that the parameters γ and κ in equation (6.3) are symmetric. In reality it is not possible to fabricate lossless rings, thus it is a question of balancing the couplings. Using the expression (6.3) and inserting the values of the FSR and the total loss in ring, the coupling coefficient κ for each resonator configuration can be found. Since the radius of curvature of the rings investigated is chosen to be above the critical bend radius, the total loss in the ring is estimated to be the propagation loss times the length of the ring.

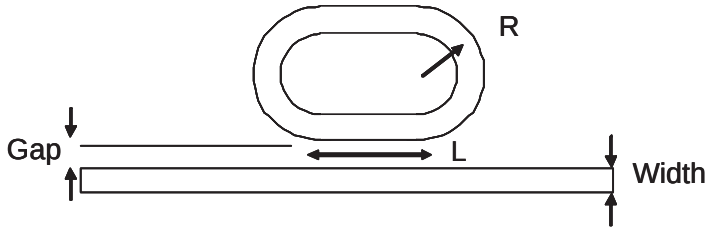

Figure 6.4: A ring resonator coupled to a straight waveguide. R is the radius of curvature, and L is the coupling length.

6.2 Measurements

The measurement setup used was similar to the one described in section 5.3. To obtain the required spectral resolution of 1 pm, for measuring resonances of rings resonators, a tunable laser in connection with the optical spectrum analyzer was used to record the narrow transmission resonance.

Structures consisting of a SRN ring coupling to a straight SRN waveguide has been studied. All the resonators are in a racetrack configuration as shown in figure 6.4. The waveguide width in the resonators as well as the straight waveguide is 1.2 μm, and the height is 0.61 μm. Although the measured waveguides are able to support higher order modes no other resonances were observed that can be attributed to other than the fundamental mode. That no higher modes are observed is due to the elevated bend loss in the resonator loop for higher order modes.

Ring resonators are polarization-dependent due to waveguide asymmetry. Even very small variations in the waveguides can give large variations (in the nm range for SRN waveguides) in the resonance wavelengths. The difference in behavior for TE and TM polarized light has been studied by Hugh Philipp [7]. The TM mode was more lossy than the TE mode.

The racetrack-shaped resonators investigates had radii varying from 29 to 100 μm. Since the radii are larger than the critical bend radius of 25 μm, the attenuation in the racetracks can be attributed to pure propagation loss. The transmission spectra were analyzed using a Lorentzian fit to each absorption peak, determining the center wavelength of the peaks, and the full width half maximum (FWHM). The FSR is the dis-

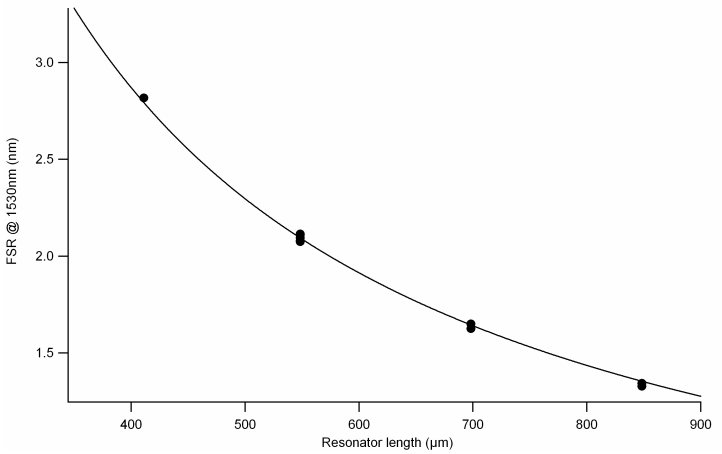

Figure 6.5: Free spectral range (FSR) as a function of ring resonator length. The symbols are the measured values; the curve is a theoretical fit [6].

tance between the center wavelengths of the peaks. In figure 6.5 the measured FSR (symbols) of the resonators is compared to the theoretical values (curve), showing good agreement. The finesse[2] of these resonators is around 65.

A transmission spectrum of a ring resonator, with a radius of 100 μm, and a separation between ring resonator and waveguide of 1.0 μm, is shown in figure 6.6. In figure 6.7 a zoom in on the transmission spectrum of two single peaks is shown. As can been seen, the distance between the resonances (the FSR) is 1.7 nm.

The fractional coupling (κ) has been calculated for two resonances in resonators with different round trip and coupling lengths. The data is displayed in table 6.1. The loss has been estimated as a propagation loss corresponding to the resonator length since the radius of curvature is above the critical 25 μm.

Different racetrack-structured resonators, with varying radius, ring, and coupling lengths have been analyzed to investigate the influence of these parameters on the fractional coupling coefficient and extinction ra-

[2]Finesse = $\frac{\text{FSR}}{\text{FWHM}}$ is a measure of the quality of the resonator.

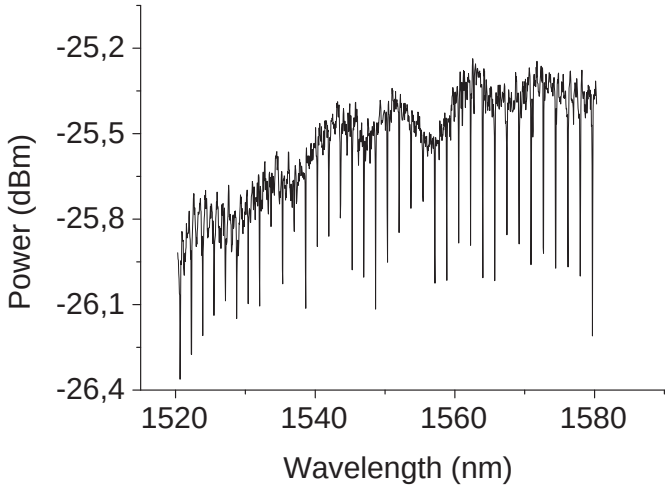

Figure 6.6: A transmission spectrum of a resonator with a radius of 100 μm, separation between resonator and waveguide is 1.0 μm [6]. The wavy nature of the spectrum is due to the behavior of the light source.

	resonator 1	resonator 1	resonator 2	resonator 2
Resonator length	548.38	548.38	698.26	698.26
FSR @1530nm (nm)	2.079	2.093	1.628	1.640
Round trip loss in dB	0.1863	0.1863	0.2374	0.2374
Fractional loss	0.0420	0.0420	0.0532	0.0532
Coupling length (μm)	175.9	175.9	34.97	34.97
Fractional coupling	0.0984	0.0896	0.00347	0.00422

Table 6.1: The fractional coupling (κ) has been calculated for two resonators with different round trip and coupling lengths [6].

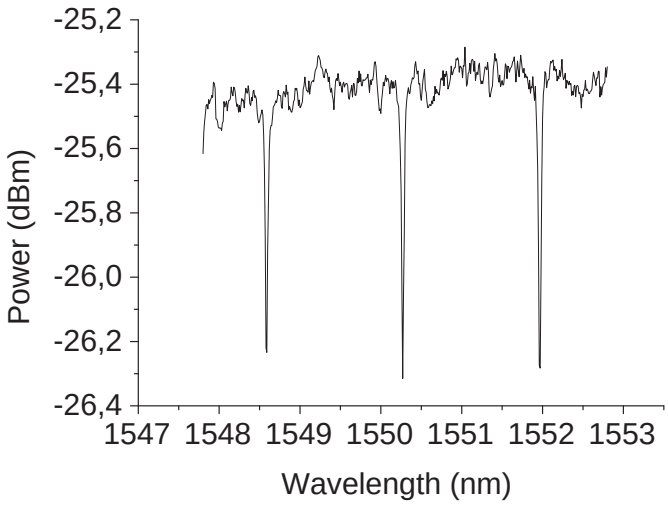

Figure 6.7: A high resolution transmission spectrum of a resonator with a radius of 100 μm, separation between resonator and waveguide is 1.0 μm. FSR = 1.7 nm at 1550 nm [6].

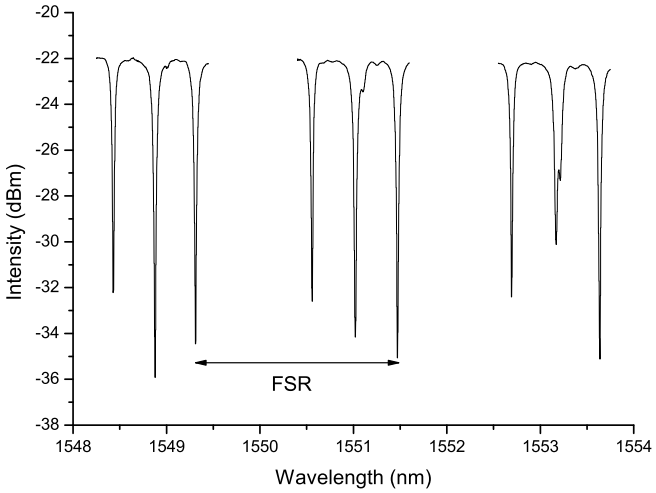

Figure 6.8: Transmission spectra of three resonators with radii of 31 μm, separation between the resonators and waveguide is 1.0 μm [6].

tio. A FSR over 30 nm for SRN ring resonators of bending radii of 6 μm has been demonstrated [8] and an extinction ratio (difference between then minimum and maximum transmitted power) of nearly 15 dB for the dropped signal has been achieved.

Structures consisting of three adjacent SRN rings coupled to a straight SRN waveguide have also been studied. When measuring on structures with three resonators, three different resonances are observed, one for each resonator, as illustrated in the spectrum in figure 6.8. The spectrum is shown for a resonator with a radius of 31 μm. The FSR is 2.14 nm and an extinction ratio of around 15 dB.

6.3 Conclusions

Micro-resonators consisting of a waveguide loop made of silicon rich nitride coupling to a straight waveguide of the same material have been investigated. A strong resonance with suitable high finesse was observed with a free spectral range of several nanometers and an extinction ratio

of nearly 15 dB for the dropped signal has been achieved. A FSR over 30 nm for SRN ring resonators of bending radii of 6 μm has been demonstrated [8]. These resonator loops are an important building block for add-drop multiplexers and digital optical filters, which proves that silicon rich nitride is a suitable platform for optical large scale integration.

Chapter 6 references

[1] C. K. Madsen and J. H. Zhao. *Optical Filter Design and Analysis: A Signal Processing Approach*. Microwave and Optical Engineering. John Wiley & Sons, Inc., July 1999. ISBN 0-471-18373-3.

[2] C. Laurent-Lund. *Multilevel integration of Optical Waveguides*. Ph.d. thesis, MIC, DTU, Denmark, august 1997. ISBN 87-89935-10-1.

[3] S. Suzuki, K. Shuto, and Y. Hibino. "Integrated-optic ring resonators with two stacked layers of silica waveguide on Si", *IEEE Photonics Technology Letters*, vol. 4, no. 11, pp. 1256–1258, 1992.

[4] W. R. Headley, G. T. Reed, A. Liu, M. Paniccia, and S. Howe. "Polarisation independent optical ring resonators on silicon on insulator", *Integrated Optics and Photonic Integrated Circuits and Proceedings of SPIE - The International Society for Optical Engineering*, vol. 5451, pp. 276–283, 2004.

[5] P. Dumon, W. Bogaerts, V. Wiaux, J. Wouters, S. Beckx, J. Van Campenhout, D. Taillaert, B. Luyssaert, P. Bienstman, D. Van Thourhout, and R. Baets. "Low-loss soi photonic wires and ring resonators fabricated with deep uv lithography", *Photonics Technology Letters, IEEE*, vol. 16, no. 5, pp. 1328–1330, 2004.

[6] K. N. Andersen, W. E. Svendsen, R. K. Sandberg, H. T. Philipp, and J. Hübner. "Silicon rich nitride micro-resonators", *11th European Conference on Integrated Optics*, vol. 1, pp. 43–6, 2003.

[7] H. T. Philipp. *High-Index Contrast Silicon Rich Silicon Nitride Waveguides and Devices*. Ph.D. thesis, Research Center COM, Technical University of Denmark, Oersteds Plads, Build. 345V, DK-2800 Kgs. Lyngby, Denmark, October 2004. ISBN 87-90974-55-7.

[8] H. T. Philipp, K. N. Andersen, W. Svendsen, and H. Ou. "Low-loss silicon rich nitride waveguides for high density integrated optics", in *Integrated Photonic Research/Optical Society of America,* p. JWB28, 2004.

Chapter 7

Conclusions

This thesis addresses the fabrication, characterization, and optimization of SRN thin film and waveguides for low loss optical components; it is part of the requirements for obtaining the Ph.D. degree at the Technical University of Denmark.

The work is divided into three parts, thin film fabrication and characterization, fabrication of waveguide structures, and characterization of optical waveguide components. The behavior of the waveguide components is strongly dependent on the thin film properties and the cleanroom fabrication, so these parameters have been optimized in order to yield components with the lowest possible optical loss and highest possible yield.

The thin film characterization consisted of determinations of stoichiometry, chemical composition, and optical loss of SRN film films. The chemical composition profile of SRN thin films on Si and SiO_2 substrates were studied using synchrotron radiation, X-ray photon spectroscopy (XPS), Rutherford backscattering (RBS), and spectral ellipsometry. The results show that the silicon content in the thin films increases with increasing DCS/NH_3 ratio in the deposition chamber gas.

Furthermore, the silicon concentration in films deposited on Si substrates increases with increasing annealing temperature. Silicon diffusion was observed throughout the thin films deposited on Si substrates when annealing was performed at temperatures above 1100 °C. Also, an intermediate layer was found between the thin film and the substrate with a linear concentration gradient of silicon. The thickness of this layer in-

creases with annealing temperature, and therefore the total amount of silicon in the film increases at the same time. The diffusion of silicon into the thin film can be prevented by growing a layer of SiO_2 on top of the Si substrate, but at the expense of triggering diffusion of oxygen from the substrate into the film.

It is noted that a SiO_2 layer between the Si substrate and the SRN film is used in optical components. Even though silicon diffusion from the substrate is eliminated by the oxide layer, there is still some diffusion of free silicon in the film. When annealing at high temperatures (above 1100 °C), the free silicon tends to collect into nano-clusters, which are expected to lead to higher optical losses. The diffusion of oxygen from the thermal oxide into the SRN films might also contribute to the optical losses due to local variations in the refractive index or absorption due to O-H bonds.

The sources of optical loss were investigated in as-deposited and annealed SRN films. A minor absorption peak was observed around 1530 nm and was attributed to the N-H absorption. The propagation loss could be lowered by annealing 1100 °C, however the absorption peak did not disappear entirely. It might be possible to remove it by annealing at even higher temperatures, but this may cause other problems such as the formation of nano-clusters. It has been observed that such clusters start to form at temperatures above 1100 °C, so this temperature seems to represent the best compromise between reducing losses due to N-H absorption and avoiding clusters, which give problems with scattering.

The second part of the project was the fabrication of optical submicron structures in SRN films. A stable, reproducible fabrication technique for processing low-stress SRN thin films and waveguides with excellent uniformity in thickness and index was developed. The stress in the SRN films was reduced to around 50 MPa through deposition and annealing optimization; stress induced birefringence can then be neglected. The cleanroom fabrication was optimized in such a way as to minimize the optical losses in waveguide structures. A process was developed for processing submicron structures with UV-photolithography and reactive ion etching. The components have 90 degree sidewalls with a roughness small enough to not induce scattering losses.

The third part of the project is a thorough analysis of SRN waveguides and components. The main focus was on minimizing the optical losses

arising from the production of the waveguide structures in the SRN thin films. Slab and channel waveguides processed under the same conditions have a propagation loss in the same range (0.7 ± 0.3 dB/cm). Since the difference in the losses is within the measurement uncertainty, it means that the processing of waveguide components is optimized to a degree where no extra losses are induced.

Further process improvement and a reduction of the number of particles has reduced the propagation loss even more from 0.73 ± 0.27 dB/cm to 0.44 ± 0.24 dB/cm at 1550 nm. This is a major achievement and is (to the knowledge of the author) the lowest loss observed for single mode buried SRN channel waveguides. Furthermore, it has been observed that the propagation loss can be lowered by 1 dB/cm (compared to as-deposited) by annealing at 1100 °C. This is seen for both slab and channel waveguides. The reason for this reduction in loss has been attributed the breaking of N-H bonds.

Experimentally, waveguide bends as small as 20 μm in curvature has proven not to induce excess loss. This bending radius is in good agreement with theoretical predictions. The bend loss is smaller than 0.1 dB per 90 degree bend for radii of curvature down to 20 μm.

Micro-resonators consisting of a waveguide loop made of silicon rich nitride coupling to a straight waveguide of the same material were also investigated. A strong resonance was observed with a free spectral range of several nanometers and an extinction ratio of 15 dB. These resonator loops are important building blocks for add-drop multiplexers and digital optical filters. Based on my results silicon rich nitride appears as a viable platform for high index contrast planar light-wave circuits with complex functionalities.

I believe that my major contribution to this promising technology has included a stable fabrication process of planar single mode submicron SRN waveguide structures. The fabrication technique of the components is realized with UV-lithography and RIE etch even though their size is just on the limit of what is possible. I have characterized the SRN films and the major optical loss contributions have been analyzed and minimized. The cleanroom fabrication has been optimized to a degree where no extra waveguide losses are induced by the processing. I have also shown that the propagation loss has the lowest observed value seen until now for SRN channel waveguides. Bend losses have also been addressed and the

experimental critical radius is in agreement with the theoretical value of 20 μm. Furthermore the performance of several ring resonators has been investigated. It was possible to achieve a FSR that was larger enough to be used WDM systems. This opens up for several new possibilities such as testing the components in a system experiments.

Appendices

Appendix A

A description of RBS

When a sample is bombarded with a beam of high energy particles, the vast majority of particles are implanted into the material and do not escape. A small fraction of the incident particles do undergo a collision with a nucleus of one of the atoms in the upper few micrometers of the sample. Energy exchange occurs because of Coulomb forces between nuclei in close proximity to each other. However, the interaction can be modelled accurately as an elastic collision using classical physics. The energy measured for a particle backscattering at a given angle depends upon two processes. Particles lose energy while they pass through the sample, both before and after a collision. The amount of energy lost is

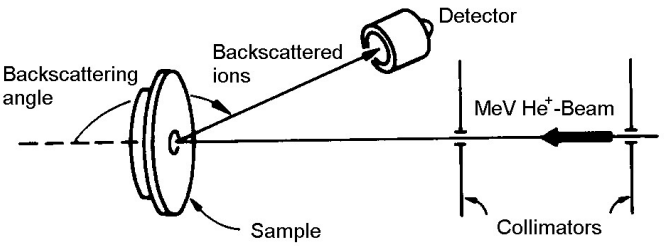

Figure A.1: RBS scattering angles [www.unibwm-physik.de]

dependent on that material's stopping power. A particle will also lose energy as the result of the collision itself. The collision loss depends on the masses of the projectile and the target atoms. The ratio of the energy of the projectile before and after collision is called the kinematic factor. The number of backscattering events which occur from a given element in a sample depends upon two factors: the concentration of the element and the effective size of its nucleus. The probability that a material will cause a collision is called its scattering cross section.

For scattering at the sample surface the only energy loss mechanism is momentum transfer to the target atom. The ratio of projectile energy immediately after scattering to incident energy immediately before scattering:

$$K = \frac{E_{scattered}}{E_{incident}} = \left[\frac{\sqrt{1 - (\frac{M_1 \sin\theta}{M_2})^2} + \frac{M_1 \cos\theta}{M_2}}{1 + \frac{M_1}{M_2}} \right]^2 \tag{A.1}$$

where E is the ion energy, M_1 the mass of the incident ion, M_2 the mass of the target atom, and θ the scattering angle. There is a much greater separation between the energies of particles backscattered from light elements than from heavy elements, because a significant amount of momentum is transferred from the incident particle to a light target atom. As the mass of the target atom increases, less momentum is transferred to the target atom and the energy of the backscattered particle asymptotically approaches the incident particle energy. This means that RBS is more useful for distinguishing between two light elements than it is for distinguishing between two heavy elements. RBS has good mass resolution for light elements, but poor mass resolution for heavy elements. However, as the mass of the atom being struck increases, a smaller and smaller portion of the projectile energy is transferred to the target during collision, and the energy of the backscattered atom asymptotically approaches the energy of the beam. An important related issue is that He will not scatter backwards from H or He atoms in a sample. This means that it is not possible to measure the amount of H in SRN samples. Elements as light as or lighter than the projectile element will instead scatter at forward trajectories with significant energy. Thus, these elements cannot be detected using classical RBS. However, by placing a detector so that these forward scattering events can be recorded, these elements can

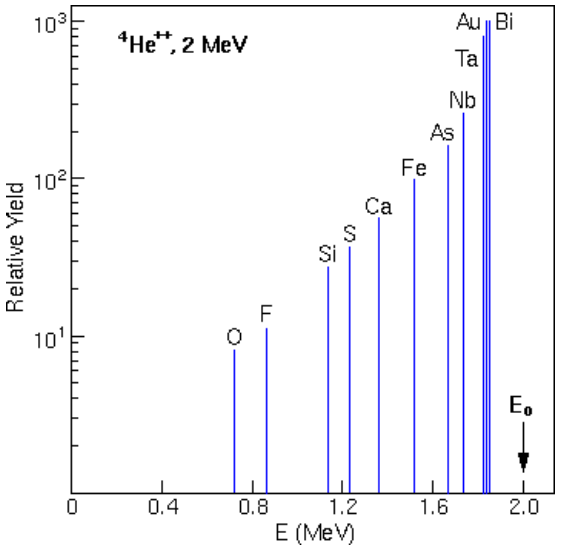

Figure A.2: Relative yield for He.

be quantitatively measured using the same principles as RBS.

The relative number of particles backscattered from a target atom into a given solid angle for a given number of incident particles is related to the differential scattering cross section. The scattering cross section is basically proportional to the square of the atomic number of the target atom.

The illustration, figure A.2, shows relative yields for He backscattering from selected elements at an incident He energy of 2 MeV. The energies for He backscattering from these elements when present at the surface of a sample are also displayed. The graph indicates that RBS is over 100 times more sensitive for heavy elements than for light elements, due to the larger scattering cross sections of the heavier elements.

Scattering cross section is the probability that a projectile will be scattered into a detector with a given solid angle.

$$\frac{\partial\sigma}{\partial\Omega} = [\frac{Z_1 Z_2 e^2}{4E}]^2 \cdot \frac{4}{\sin^4\theta} \cdot \frac{[\sqrt{1-(\frac{M_1\sin\theta}{M_2})^2}+\cos\theta]^2}{\sqrt{1-(\frac{M_1\sin\theta}{M_2})^2}} \qquad \text{(A.2)}$$

Z_1 is the atomic number of incident ion, Z_2 the atomic number of

target atom, E energy of incident ion, M_1 the mass of incident ion, M_2 the energy of target atom and θ is the angle of incidence.

Only a small fraction of the incident particles undergo a close encounter with an atomic nucleus and are backscattered out of the sample. The vast majority of the incident He atoms end up implanted in the sample. When probing particles penetrate to some depth in a dense medium, projectile energy dissipates due to interactions with electrons (electronic stopping) and to glancing collisions with the nuclei of target atoms (nuclear stopping). This means that a particle which backscatters from an element at some depth in a sample will have measurably less energy than a particle which backscatters from the same element on the sample surface. The amount of energy a projectile loses per distance traversed in a sample depends on the projectile, its velocity, the elements in the sample, and the density of the sample material. Typical energy losses for 2 MeV He range between 100 and 800 eV/nm. This energy loss dependence on sample composition and density enables RBS measurements of layer thicknesses, a process called depth profiling. The majority of energy loss is caused by electronic stopping which behaves (roughly) like friction between the probing particles and the electron clouds of the target atoms. Nuclear stopping is caused by the large number of glancing collisions which occur along the path of the probing atom. Nuclear stopping contributes significant energy losses only at low particle energies. The ratio of energy loss to two-dimensional atom density for a given material is known as its stopping cross section. Since the majority of energy loss is caused by interactions with electrons, the electronic structure of the target material has a significant affect upon its stopping power. Theoretical predictions of stopping power are both complicated and inaccurate. Therefore, empirical stopping powers are often used in RBS calculations. A polynomial equation and a table of coefficients provide calculations of stopping powers over a wide range of energies and elements. In order to calculate the energy loss per unit of depth in a sample one can multiply stopping cross section times the density of the sample material (atoms/cm^2). Sample densities can vary significantly. It is necessary to know the density of the sample material in order to calculate the depth of a feature or the thickness of a layer by RBS. More information on RBS can be found in [1].

By measuring the energy width of the Si peak or the N step and dividing by the energy loss of He per unit depth in a SiN matrix, the

thickness of the SiN layer can be calculated.

By measuring the height of the Si and N peaks and normalizing by the scattering cross section for the respective element, the ratio of Si to N can be obtained at any given depth in the film. The stopping cross section for SiN is significantly higher than for pure N. This means that a backscattered particle will lose more energy per unit volume in SiN than in pure N. An implication of this fact is that, for a given energy loss, there are fewer atoms contained in a volume of SiN than for the same volume of pure N. This results in fewer backscattering events, and that means the peak for silicon will be lower in the SiN than in the pure N layer.

The height of a backscattering peak for a given layer is inversely proportional to the stopping cross section for that layer. The stopping cross section of SiN is known to be only 1.37 times that of N. This explains why the height of the peak corresponding to N in the SiN layer is less than one-half the height of the peak corresponding to Si in the substrate.

It is also possible to calculate the Si concentration in the SiN film by comparing the height of the Si peak for the SiN layer to that of the peak for the pure Si substrate, but only after correcting for the different stopping cross sections of the two materials.

Particles lose energy as they traverse the sample, either through encounters with electrons or with nuclei of individual atoms. Since this process occurs one atom at a time, a given encounter is not affected by any previous encounters or by any following encounters. This means that if the stopping cross sections for each element are known, then the stopping cross section for a compound sample can be calculated simply by multiplying the stopping cross section for each element by its concentration.

The different bonding states which can be present in compounds often cause deleterious effects for other analytical methods such as SIMS or AES, but due to the high energy of the probing particles with RBS compared to the very small (few eV) binding energies, this is not a problem for RBS. This is one of the reasons that quantitative RBS analysis can usually be performed without the use of standards for calibration.

Appendix A references

[1] M. Ohring. *The Materials Science of Thin Films.* Academic Press, Inc., 1992. ISBN 0-12-524990-X.

Appendix B

A description of XPS

The samples are irradiated with monochromatic X-rays which cause the ejection of photoelectrons from the surface. The typical energy of the photoelectron beam is above 1 keV. The electron binding energies, as measured by a high resolution electron spectrometer, are used to identify the elements present and, in many cases, provide information about the valence state(s) or chemical bonding environment(s) of the elements thus detected. The penetration depth and thereby the probe depth of the surface, typically the outer most 3 nm of the sample, is determined by the escape depth of the photoelectrons and the angle of the sample plane relative to the spectrometer. One of the unique advantages of XPS is that it is a convenient and quick elemental analysis of surfaces. It is possible to determine the valence states and/or bonding environment of atoms near the surface. Characterization of very thin surface layered structures is also one of the advantages of this method. Furthermore, a depth profile of both conducting and insulating materials can be performed using the attached Ar-ion sputtering equipment.

The relative peak areas can be expressed as percentages of a defined total while at the same time compensating for the cross sections (relative sensitivity) of the various peaks. This gives a better representation of the true amounts of material present. Elements can have vastly different cross section sp two peaks representing two elements will have a very different area for the same amount of the material in the sample. Quantification requires that the peaks in the table in the program be associated with entries in a database containing the element characteristic line and its

sensitivity factor. One has to scan through the database if the elements have experienced large chemical shifts or they are satellite lines. Satellite peaks occur for most peaks because X-rays are not monochromatic. The satellite peaks are due to Bremsstrahlung radiation, less probable transitions (e.g. Kβ; valence band $\rightarrow$ 1s) or transitions in a multiply ionized atom (e.g. Ka3,4). It is necessary to use the curve fitting function in order to provide better quantification data either to resolve overlapping peaks or to simply give a more accurate peak area. More information on XPS and the analysis of the spectra can be found in [1].

Appendix B references

[1] D. Briggs and M. P. Seah. *Practical Surface Anaylsis: Auger and X-ray Photoelectron Spectroscopy*, vol. 1. John Wiley & Sons, Chichester, England, Second edition, 1996. ISBN 0-471-95340-7.

Appendix C

Wave equation

Classical electromagnetism describes the behavior of optical waveguides. The electric displacement **D**, the electric field **E**, the magnetic flux density **B**, and the magnetic field **H** are vectorial quantities, with a dependence described through the Maxwell equations:

$$\nabla \cdot \mathbf{D} = 0 \tag{C.1}$$

$$\nabla \cdot \mathbf{B} = 0 \tag{C.2}$$

$$\nabla \times \mathbf{H} = \frac{\partial}{\partial t}\mathbf{D} \tag{C.3}$$

$$\nabla \times \mathbf{E} = -\frac{\partial}{\partial t}\mathbf{B} \tag{C.4}$$

For a linear isotropic medium:

$$\mathbf{D} = \epsilon \mathbf{E} \tag{C.5}$$

$$\mathbf{B} = \mu \mathbf{H} \tag{C.6}$$

where ϵ is the permittivity[1] and μ is the permeability[2]. For waveguides the description is much more complicated, but if they are passive it can be assumed that ideally the permittivity is independent of time. Assuming this and taking the curl of equation (C.4), the above equations can be written as [1], [2]:

[1] $\epsilon = \epsilon_r \epsilon_0$, where ϵ_0 is the vacuum permittivity and ϵ_r is the relative permittivity.

[2] $\mu = \mu_r \mu_0$, where μ_0 is the vacuum permeability and μ_r is the relative permeability.

$$\begin{aligned} \nabla^2\mathbf{E} - \mu\epsilon\frac{\partial^2}{\partial t^2}\mathbf{E} &= \nabla(\nabla\cdot\mathbf{E}) \\ &= -2\nabla(\nabla\ln(n)\cdot\mathbf{E}) \end{aligned} \tag{C.7}$$

where n is the refractive index and is $\sqrt{\epsilon_r}$. The left hand side is the wave equation and the right hand side is a consequence of the refractive index being a function of the spatial variables. For waveguides with a small index contrast the right hand side can be approximated by zero [1]. This is what is the so called weak guiding approximation. For SRN waveguides the index contrast is much higher and therefor the right hand term can not be assumed to be negligible across the waveguide cross section.

In an idealized model of the waveguide the refractive index of the waveguide is a step function. This makes the natural log of the index undefined at the boundary. A general solution can be found for the constant refractive index model, and the boundary conditions can be applied later [1]. If the optical axis of the waveguide is taken to be the z-direction, then the x and y coordinates are transverse with respect to the propagation direction. Equation (C.7) can then be written as [1]:

$$\nabla_t^2\mathbf{E} + k_0^2 n^2\mathbf{E} = \beta^2\mathbf{E} \tag{C.8}$$

where $k_0 = \frac{2\pi}{\lambda}$ is the magnitude of the wave vector, β is the propagation constant[3], and ∇_t is:

$$\nabla_t^2 = \frac{\partial^2}{\partial x^2} + \frac{\partial^2}{\partial y^2} \tag{C.9}$$

Equation (C.8) is an eigenvalue equation with eigenvalue β^2 and eigenvector $\mathbf{E}(x, y)$. A similar equation can be derived for $\mathbf{H}$. For waveguides with square cross sections there are no know analytical solutions to these equations satisfying the boundary conditions. Approximations (e. g. Marcatili approximation [3]) and numerical techniques (e. g. finite difference [4], and wave matching method [5]) are generally used to find a solution.

[3] β is defined by assuming $\mathbf{E}(x, y, z) = \mathbf{E}(x, y)\cdot e^{-i\beta z}$.

From the solutions β, or the effective index ($n_{eff} = \beta/k_0$), for any given mode, and detailed information on the mode profile is found. The discrete set of effective indices that is found correspond to different propagating modes. From the boundary conditions it is found that for guided modes the effective indexes has to fulfill: $n_{clad} > n_{eff} > n_{core}$, where n_{clad} and n_{core} is the refractive index of the core and cladding respectively. This means that for high index waveguides there is a much larger range of effective indexes associated with guided modes than for low index waveguides.

For optical telecommunication purposes single mode waveguides are desired in order to avoid problems with modal dispersion, which leads to degradation of the signal. For only one mode to be guided the waveguide core has to be designed so small that only the fundamental mode is a solution to the eigenvalue equation (C.8).

Appendix C references

[1] F. Ladouceur and J. D. Love. *Silica-based Buried Channeal Waveguides and Devices*. Optical and quantum electronics series. Chapmann & Hall, London, 1996. ISBN 0-412-57930-8.

[2] M. Born and E. Wolf. *Principles of optics*. Cambridge University Press, Cambridge, 7th edition, 1999. ISBN 0-521-64222-1.

[3] E. A. J. Marcatili. "Dielectric rectangular waveguide and directional coupler for integrated optics", *Bell System Technical Journal*, vol. 48, no. 7, pp. 2071–102, 1969.

[4] K. Okamoto. *Fundamentals of Optical Waveguides*. Optics and Photonics. Academic Press, February 2000. ISBN 0-12-525095-9.

[5] M. Lohmeyer. "Vectorial wave-matching mode analysis of integrated optical waveguides", *Optical and Quantum Electronics*, vol. 30, no. 5, pp. 385–396, 1998.